Electronic Supplementary Material (ESI) for Analyst.

This journal is © The Royal Society of Chemistry 2016

Supporting Information

Metal oxide semiconductor SERS-active substrate by defect engineering

Hao Wu, Hua Wang and Guanghai Li*

1. General consideration

According to Herzberg-Teller theory,[1-3] when the highest occupied molecular orbital (HOMO) energy level and the lowest unoccupied molecular orbital (LUMO) energy level of the attached molecules are matched to the conduction band (CB) and valence band (VB) of a semiconductor substrate and the incident laser, thermodynamically allowed PICT process will occur between the substrate and the absorbed molecules. The transfer changes the position of the atomic nucleus and the potential in the molecule.[4] After coming back of the electrons through the vibronic coupling of the states in the molecules and the substrate, the polarizability tensor of the absorbed molecules will be magnified, which will enhance the Raman scattering. Since the enhancement of the molecular polarizability tensor in a semiconductor-molecule system is originating from the PICT process,[5, 6] an efficient PICT process between the absorbed molecules and substrate is crucial to realize SERS activity for a non-SERS-active substrate.

There are two important qualifications to transfer a non-SERS active substrate to a SERS-active one with an optimal SERS performance when molecules are closely attached to the substrate. First, the energy levels of substrate and the absorbed molecules must match with the excitation light. Second, the PICT efficiency which determines the SERS performance must be high enough in each specific PICT process.

It is widely assumed that vacuum levels will align when molecules are attached to the substrate, and upon which the SERS is explained. While recent study has proved that the vacuum levels do not always align when molecules are attached on the substrate,[7-9] in which the HOMO or LUMO levels of the molecules are pinned to the Fermi level (E_F) of the substrate and leaving a vacuum level offset between the substrate and molecules. When molecules are tightly adsorbed on the substrate, electrons can transfer spontaneously between the molecules and the substrate. If the work function Φ (energy difference between the E_F and the vacuum level) of the substrate is smaller than the electron affinity *EA* (energy difference between the LUMO level and the vacuum level) of the molecules, electrons can transfer from the available partially occupied (or fully occupied) levels in the substrate near (or above) the LUMO level to the molecules under thermal excitation, in this case the LUMO level will be pinned above the E_F (separated by a energy difference of about 0.1 eV), which makes the local vacuum level of the molecules becomes higher than that of the substrate, as shown in M_{11} of Scheme S1d. If the work function Φ of the substrate is larger than the ionization energy *IE* (energy difference between the HOMO level and the vacuum level) of the molecules, and there exist partially occupied (or empty) levels in substrate near (or under) the HOMO level under thermal excitation, electrons will transfer from the molecules to these partially occupied (or empty) levels, and the HOMO level will be pinned under the E_F (separated by a energy difference of about 0.3 eV), which makes the local vacuum level of the molecules becomes lower than that of substrate, as shown in M_{12} of Scheme S1d. When work function Φ is larger than *IE* but smaller than *EA* (Scheme S1a), or no energy levels in substrate are available to accept or offer electrons under thermal excitation (Scheme S1b), or the molecules are not

closely adsorbed on substrate (Scheme S1c), no electrons will transfer spontaneously, and the vacuum level of the molecules will align with substrate.

In the case shown in Scheme S1c, because there is neither the spontaneous electron transfer nor SERS effect based on the PICT process, it will not be discussed in this paper. While in the cases shown in Scheme S1a, b and d, the molecules are closely attached to substrate. Only if the photon energy (hv) is larger than the energy difference between HOMO and LUMO ($hv>E_{LUMO}$-E_{HOMO}) and hν>E_{cm}-E_{HOMO}, or hv is larger than the bandgap of the substrate ($hv>E_{cm}$-E_{vm}), the energy levels of both the substrate and molecule will match with the excitation laser, and thus a notable SERS effect from the PICT process can be observed.

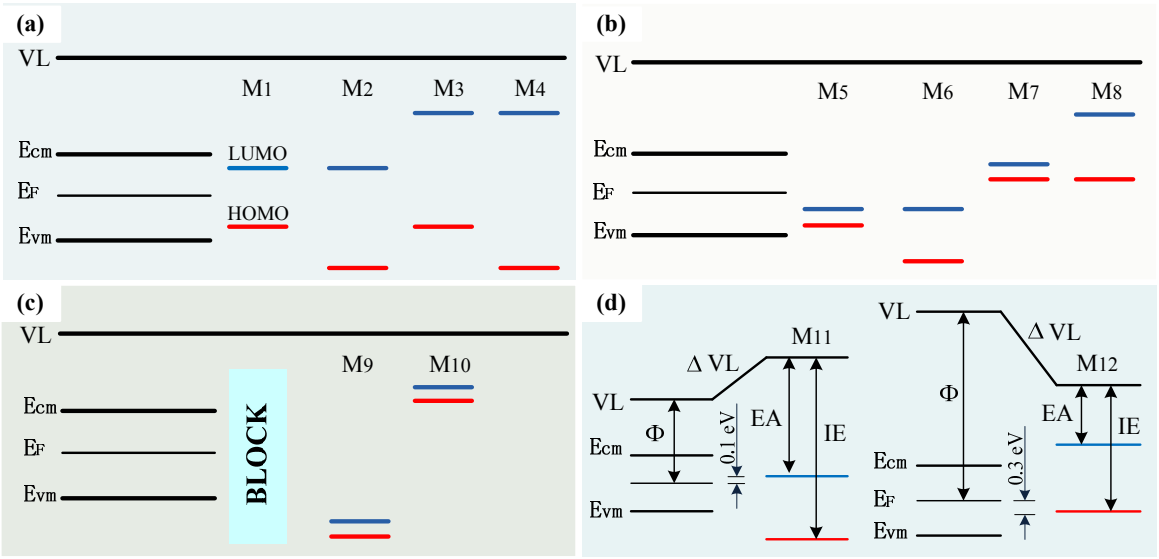

Scheme S1. Energy diagrams for a semiconductor substrate and the adsorbed molecules (E_{cm}, conduction band minimum; E_F, Fermi level; E_{vm}, valence band maximum. M_i (i=1, 2, 3...), molecule; E_{et}, the thermal energy of the electron, ~0.03eV). The olive line represents LUMO level and the red line represents HOMO level. Vacuum level of molecule and substrate align when (a) $EA<\Phi<IE$, (b) E_{LUMO}- $E_{vm}>E_{et}$ in M_5 and M_6; E_{cm}-$E_{HOMO}>E_{et}$ in M_7 and M_8, (c) the molecules are not closely adsorbed on substrate. M_9 and M_{10} are chosen randomly. (d) $\Phi<EA$ and E_{LUMO}-$E_{vm}< E_{et}$ in M_{11}; $\Phi>IE$ *and* E_{cm}-$E_{HOMO}<E_{et}$ in M_{12}. When M_{11} and M_{12} are tightly adsorbed on the substrate, spontaneous electron transfer occurs and the vacuum levels of the substrate and the molecule are not equal.

Whether the energy levels (the energy levels of substrate and the absorbed molecules) match with the excitation light will depend on hv, the values of E_{cm}-E_{vm}, E_{LUMO}-E_{HOMO} and E_{cm}-E_{HOMO} after considering the above-mentioned possible realignment of the energy levels. When the energy levels of the substrate match with that of the absorbed molecules and the excitation light, the first qualification is fulfilled and the PICT process will occur, and if the energy levels of the substrate do not match with the molecules under certain excitation light, the PICT process is impossible, and in this case, the establishment of new energy levels in the substrate is needed to match with molecular levels and the excitation light. Decreasing E_{cm} or increasing E_{vm} will result in the match of the energy levels, which will transfer a non-SERS substrate to a SERS active one or increase the enhancement factor. Doping and introducing defects can introduce new energy levels in the bandgap of semiconductor substrate, as shown in Scheme S2, which will decrease E_{cm} or/and increase E_{vm}. In this study we will focus mainly on an increase in E_{vm} level by defect engineering, i.e. the defect levels of E_{V1} or E_{V2} shown in Scheme 2. It is worth noticing that the introduction of new energy levels might change the position of Fermi level and create new energy levels for spontaneous electron transfer between the substrate and the adsorbed molecules, which will change the pattern of energy alignment described above and therefore the matching relations need reconsideration. On the other hand, theoretically, new energy levels introduced from the surface species, defects and doping with other elements can locate anywhere under the vacuum level. In this sense, the energy levels of a semiconductor substrate can match with any molecule and excitation light wavelength.

The next qualification is to optimize the SERS performance by promoting PICT efficiency, which can be described by different PICT processes of a semiconductor-molecule system. In previous studies,[5, 6, 10] the PICT model has evolved from Lombardi's model in the metal-molecule system,[3, 11] and this model focused mainly on the magnification of polarization tensor induced by the PICT process between vibration states, and can be used to explain the SERS mechanism, but could not describe the SERS enhancement quantificationally. Computer simulation can provide a much more detailed and quantificational description of the SERS process though, it cannot give a universal guidance for different substrates and molecules considering its complication and sensitive dependence on the parameters of specific substrate and molecule in the simulations. Therefore, design a universal model that not only can describe general conditions regardless the substrate and the absorbed molecule, but also can reflect the influence of a specific factor in a specific case is essential. Here we propose a model named "effective electric current model" that reflects how the electric current involved in the PICT affecting the SERS signals by considering the influence of the defect levels in the bandgap of the substrate.

In our model, we focus on the cases where the defect concentration of the substrate is relatively low and the introduced levels act as E_{V2} in Scheme S2, i.e. defects act as donors. Since $h\nu<E_{cm}-E_{vm}$ for the intrinsic semiconductor considered here and $h\nu>E_{cm}-E_{vm}$ after introducing E_{V2}, the original valence band can be considered to be totally occupied under the excited light. Therefore the photo-excited electron transition and recombination in the original valence band can be ignored, and the primary photo-excited electron transition and recombination are relevant to E_{V2}. As electrons transfer between the substrate and the adsorbed molecules is by resonant tunneling, not all the matching levels transfer electrons. On the other hand, the electron transfer will always accompany with electron-electron and electron-phonon interaction, leading to the change in the electronic energy. In our model this transfer process is simplified as a sustained transfer current between the substrate and the adsorbed molecules with a transmission coefficient $T_{BW}(E)$ and a tiny critical offset $|\gamma|$ between the highest involved energy levels in the conduction band of the substrate and molecular LUMO as a criterion of dividing different PICT stages. We assume $\gamma=0$ for simplification and highlight the key points. This assumption does not affect the main conclusion of the model, and the γ value can be obtained from the comparison between the model and the experimental results, which in turn can be used to amend our model (see details in Part 2 of SI).

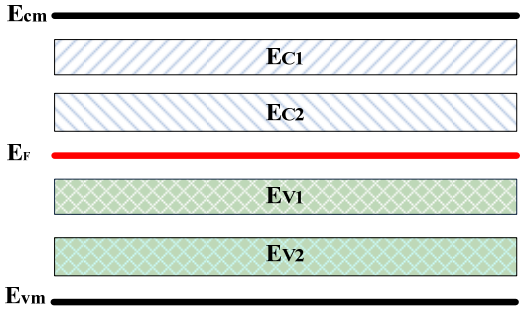

Scheme S2. Schematic defect levels in the bandgap of a semiconductor. E_{C1} and E_{C2} can be regarded as new conduction bands (i.e. a decreased E_{cm}), and E_{V1} and E_{V2} can be regarded as new valence bands (i.e. an increased E_{vm}).

The possible PICT process can be divided into three sub-PICT processes, as shown in Scheme S3, i.e., CT_1, CT_2 and CT_3. Actual PICT process consists of one to three of these sub-PICT processes. The positions of LUMO and HOMO in Scheme S3 are chosen randomly, corresponding to the case of M_3, M_4, M_8 and M_{12} in Scheme 1. Other cases are similar and will be discussed at the end of this section.

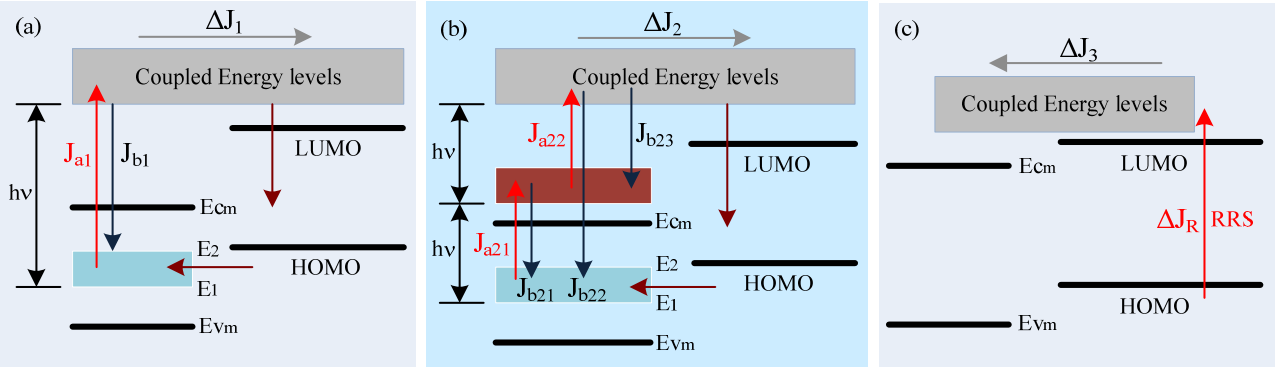

Scheme S3. Schematic schemes of three sub-PICT processes. (a) CT_1, (b) CT_2 and (c) CT_3. E_1 and E_2 are the lowest and the highest occupied defect level, respectively; $h\nu$ the energy of excitation photon. ΔJ_i (i=1 and 2) is the current injected from the substrate onto molecular levels above the LUMO in the corresponding sub-PICT process, and ΔJ_3 is the current injected from the molecular levels above the LUMO onto the energy levels in the conduction band of the substrate in the CT_3.

The electrons in defect levels will jump onto the higher levels in the conduction band of the substrate which coupled with molecular levels above LUMO when the photon energy is high enough, i.e. $h\nu>E_{cm}-E_2$ and $h\nu>E_{LUMO}-E_2$. In this case the CT_1 process takes place as shown in Scheme S3a. These excited electrons (apart from those transiting to valence band to be recombined, J_{b1}) will then transfer to the molecular energy levels above LUMO (ΔJ_1) through the vibronic coupling of energy levels and magnify the molecular polarizability tensor, resulting in the SERS effect. Most of the excited electrons are involved in the sub-PICT process directly or recombined in the substrate. The electrons jumping to even high energy levels by absorbing another photon are rare and can be ignored, therefore only a single transition process (J_{a1}) is considered here. In this case the excited electrons (J_{a1}) are either involved in the sub-PICT process (ΔJ_1) or recombined with the holes on the defect levels in the bandgap of the substrate (J_{b1}). In the CT_1 process, it is the PICT resonance between the defect levels and the coupled molecular levels above LUMO that results in the SERS effect.

In the CT_2 process, the photon energy is relatively small, i.e. $h\nu>E_{cm}-E_2$ but $h\nu<E_{LUMO}-E_2$ *and* $2h\nu>E_{LUMO}-E_2$, and above mentioned J_{a1} is impossible. In this case the electrons can firstly jump from the defect levels onto the uncoupled energy levels (the brown zone in Scheme S3b) in the conduction band of the substrate through absorbing a photon (J_{a21}). Since these energy levels are not coupled with the molecular levels above the LUMO, the electrons on these levels cannot transfer to the molecules through the vibronic coupling of energy levels and thus the occupation on these levels is high enough to be taken into account. These electrons (apart from those transiting to valence band to be recombined, J_{b21}) can jump onto the higher levels (the coupled energy levels in Scheme S3b) in the conduction band of the substrate through absorbing another photon (J_{a22}), which coupled with molecular levels above LUMO. In this case, the path to the molecules is available on these coupled levels, and the electrons will transfer to the molecules (ΔJ_2) or be recombined (J_{b22}, J_{b23}). Because of the absence of the CT_1, the CT_2 is predominant owing to a considerable occupation on the uncoupled energy levels in the conduction band (the brown zone in Scheme 3 (b)). It is the PICT resonance between the uncoupled energy levels in the conduction band of the substrate and the coupled molecular levels above LUMO that causes the SERS effect. It is worth noticing that although the CT_2 involves two excitation processes, it is not a two-photon absorption process. The contribution of two-photon absorption to SERS using a normal laser source is negligible.

The electrons involved in ΔJ_2 has a smaller number but is more sensitive to the defect concentration than those involved in ΔJ_1 because there are two extra recombining transitions of J_{b21} and J_{b23} (both affected by the occupation of defect energy levels) in the CT_2, apart from the common recombining transition J_{b22} (corresponding to J_{b1} in the CT_1). The CT_1 and CT_2 require the transition from valence band to conduction band of the substrate, thus one of the two conditions in the first qualification mentioned above is $h\nu>E_{cm}-E_{vm}$. Being having a relatively

high efficiency, the introduction of the CT_1 into the non-CT_1 PICT process will significantly enhance SERS signals.

When the photon energy is high enough to pump electrons from molecular HOMO to LUMO ($h\nu > E_{LUMO}-E_{HOMO}$), molecular resonance Raman scattering (RRS) (shown in Scheme S3c) will take place, and additional electrons ΔJ_R are excited inside the molecules, which will magnify the polarization tensor of the molecules. Molecular RRS is not a PICT process and is independent of the substrate, but it contributes to the sub-PICT process of the CT_3 when the photon energy is adequate to pump electrons from molecular HOMO to the conduction band ($h\nu > E_{cm}-E_{HOMO}$). The CT_3 is originating from the vibronic coupling between the molecular excited states and the conduction band states of the substrate (ΔJ_3, Scheme S3c), resulting in the SERS effect, in which the excited electrons on the molecular energy levels above LUMO can transfer to the coupled energy levels in the conduction band or other partially occupied (or empty) defect levels (E_{C1} or E_{C2} in Scheme S2) in the band gap of the substrate through resonant tunneling. The ΔJ_R process is enlarged by the CT_3 (ΔJ_3), further amplifying the molecular Raman signals. Since the defects in the semiconductor substrate act as donors, the CT_3 involves neither E_{C1} nor E_{C2} in the systems considered, ΔJ_3 is a constant. Therefore the SERS signal intensity in CT_3 (I_3) is independent of defect concentration. On the other hand, if the defects act as acceptor, CT_3-involved defect levels in the bandgap of the substrate act as new conduction band (E_{C1} or E_{C2} in Scheme S2), thus the corresponding PICT process is very complex, which will not be discussed in this paper. Since the CT_3 requires the transition from molecular levels under HOMO to molecular levels above LUMO and the bottom of conduction band, one of the conditions in the first qualification mentioned above is $h\nu > E_{LUMO}-E_{HOMO}$ and $h\nu > E_{cm}-E_{HOMO}$.

The above CT_1 and CT_2 correspond to the substrate-to-molecule PICT process, while the CT_3 corresponds to the molecule-to-substrate PICT process in previous studies.[5, 6, 10, 12] For the molecules in the case of M_1, M_2, M_5, M_6, M_7 and M_{11} shown in Scheme S1, our model still holds. In these cases, there are three differences compared to the situations mentioned above. First, all the electrons pumped from the valence band to the conduction band can be involved in CT_1 and recombination process, thus CT_2 disappears. Second, when $h\nu > E_{LUMO}-E_{HOMO}$ and $h\nu < E_{CM}-E_{HOMO}$, the CT_3 disappears (assuming $\gamma=0$, and the result can be amended by actual γ value). Third, for the energy level realignment, the LUMO level of M_{11} is pinned above the E_F (separated by a energy difference of about 0.1 eV), while the HOMO level of M_{12} is pinned under the E_F (separated by a energy difference of about 0.3 eV), see detail description in Part 1 of SI.

2. Theoretical model and applications

Suppose the defect levels act as new valence band and the defect concentration is relatively low. Being providing electrons (or accepting holes), these defect levels become recombination centers for electrons and holes in the PICT process. Here we ignore the Auger recombination and focus mainly on the recombination on defect levels in the bandgap. At low defect concentration, many properties of the substrate, like the energy band structure, lattice structure and adsorptivity, can be considered to be invariant with the defect concentration. The increasing process at turning on the laser and the decaying process at turning off the laser of the photoelectron are not considered here. Our effective electric current model focuses mainly on the stable state of the system with constant laser input, where the principle of detailed balance can be satisfied, in which the influx rate equals to the efflux rate of the electrons on every energy level in the substrate and molecules.

The density of defect states M_t can be obtained by summing up all the contributions from the forbidden band

$$M_t = \int_{E_1}^{E_2} N_t(E)dE \tag{S2-1}$$

where $N_t(E)$ is the energy dependent density of available defect states. E_1 and E_2 are respectively the energy value of the lowest and the highest defect level, and are constants at low defect concentration.

After absorbing a photon, electron will transit onto a higher (the stimulated absorption) or a lower (the stimulated emission) energy levels. The energy difference between the initial level and the final level of the

transition equals to the photon energy. The transition probability of the stimulated absorption and emission is the same, which is described as B_{21}, in which the subscript stands for the electron transits from energy level 2 to energy level 1. Considering the radiation field of the incident light as perturbation, the Hamiltonian of the system can be expressed as

$$\mathbf{H} = \frac{1}{2m}(\mathbf{P} - e\mathbf{A})^2 + V(\mathbf{r}) \tag{S2-2}$$

where m is electron mass, $\mathbf{P}$ the electron momentum, e the electron charge, $\mathbf{A}$ the vector field of the radiation field of the incident light, $V(\mathbf{r})$ the lattice periodic potential changing with spatial coordinate $\mathbf{r}$. Using $\mathbf{P}=-i\hbar\nabla$, equation (2) can be expressed as

$$\mathbf{H} = -\frac{\hbar^2}{2m}\nabla^2 + V(\mathbf{r}) + \frac{ie\hbar}{m}\mathbf{A}\cdot\nabla + \frac{e^2\mathbf{A}^2}{2m} \tag{S2-3}$$

and the Hamiltonian of the perturbation potential can be expressed as

$$\mathbf{H}' = \frac{ie\hbar}{m}\mathbf{A}\cdot\nabla + \frac{e^2\mathbf{A}^2}{2m} \tag{S2-4}$$

Therefore, in the stable state of constant perturbation B_{21} can be expressed as

$$B_{21} = \frac{\pi}{2\hbar}\left|\left\langle \Psi_2^*(\mathbf{r})\middle|\mathbf{H}'\middle|\Psi_1^*(\mathbf{r})\right\rangle\right|^2 \tag{S2-5}$$

where $\Psi_2(\mathbf{r})$ and $\Psi_1(\mathbf{r})$ are the electron wave function in the initial state and the hole wave function in the final state of the transition, respectively.

For each given incident laser, $\mathbf{A}$ is constant and can be labeled with the wavelength of the incident light. After the integration, $\mathbf{r}$ disappears. Therefore, the probability of the stimulated transition for electrons in a given semiconductor substrate relates only to the wavelength of the incident light, the initial and final states of the transition. Considering the fact in the stimulated transition the energy difference between the initial and final states of the transition equals to the photon energy, and the electron transition of the stimulated absorption and emission has the same probability. The probability of the stimulated transition is expressed as $B_{\lambda,s}(E)$, in which the subscript λ indicates the wavelength of the incident light, s indicates the transition in the substrate, and E indicates the lower energy of the two states in the transition.

Besides the stimulated transition, electrons in the semiconductor substrate can also transit to state with a lower energy by spontaneous transition. The probability of spontaneous transition from energy level 2 to energy level 1 (A_{21}) is irrelevant to the incident light and can be expressed as

$$A_{21} = \frac{\pi}{2\hbar}\left|\left\langle \Psi_2^*(\mathbf{r})\middle|\mathbf{H}_0\middle|\Psi_1^*(\mathbf{r})\right\rangle\right|^2 \tag{S2-6}$$

where $\mathbf{H}_0$ is the intrinsic Hamiltonian of the system, $\mathbf{H}_0 = -\hbar^2(2m)^{-1}\nabla^2 + V(\mathbf{r})$. A_{21} relates to the energy of the initial state and final state of the transition, and can be rewritten as $A_s(E,E')$. The subscript s indicates that the electrons transits in the semiconductor substrate. E and E' represent the energy of the initial state (the higher level) and the final state (the lower level) in the transition, respectively. In the model we suppose all the defect levels are involved in the PICT process, which does not always fulfill in reality, an amendment will made by introducing a function as described in the application part.

The CT_1 process

When the photon energy is high enough, i.e. $h\nu > E_{cm} - E_2$ and $h\nu > E_{LUMO} - E_2$, the CT_1 process takes place. After absorbing a photon with an energy of $h\nu$, electrons on the defect levels can transit onto the levels in the conduction band of the substrate coupled with the molecular levels above LUMO with the transition current J_{a1}. If $F_{sL}(E)$ and $F_{sH}(E+h\nu)$ are respectively the electron distribution function on the defect levels and on the coupled levels in the conduction band of the substrate ($E_1<E<E_2$), $N_{sc}(E+h\nu)$ is the density of the coupled levels in the conduction band of the substrate ($E_1<E<E_2$), J_{a1} will be proportional to the density of the filled initial levels $N_t(E)F_{sL}(E)$ and the

density of the unfilled final levels $N_{sc}(E+h\nu)[1-F_{sH}(E+h\nu)]$. The scale coefficient is the probability of the stimulated transition $B_{\lambda,s}(E)$ and electron charge e. Therefore, the transition current J_{a1} can be expressed as

$$J_{a1} = e\int_{E_1}^{E_2} B_{\lambda,s}(E)N_t(E)F_{sL}(E)N_{sc}(E+h\nu)[1-F_{sH}(E+h\nu)]dE \tag{S2-7}$$

The unit of $B_{\lambda,s}(E)$ is Jm^3s^{-1}, and that of $N_t(E)$ and $N_{sc}(E+h\nu)$ are $m^{-3}J^{-1}$. J_{a1} is the current of the excited electrons within unit volume, and in unit of $Cs^{-1}m^{-3}$.

The electrons excited to the coupled levels in the conduction band of the substrate can be recombined in two routines: spontaneous transition and stimulated emission. The spontaneous transition current of the electrons on each energy level is proportional to the density of the filled initial levels $N_{sc}(E)F_{sH}(E)$ and the density of the unfilled final levels $N_t(E')[1-F_{sL}(E')]$ ($E_1+h\nu<E<E_2+h\nu$, $E_1<E'<E_2$). The scale coefficient is the probability of spontaneous transition $A_s(E,E')$. By sum up all the contribution of the electrons on the higher levels, the spontaneous transition rate can be expressed as

$$\int_{E_1+h\nu}^{E_2+h\nu}\int_{E_1}^{E_2} A_s(E,E')N_{sc}(E)F_{sH}(E)N_t(E')[1-F_{sL}(E')]dE'dE$$

The stimulated emission is proportional to the density of the filled initial levels $N_{sc}(E+h\nu)F_{sH}(E+h\nu)$ and the density of the unfilled final levels $N_t(E)[1-F_{sL}(E)]$ ($E_1<E<E_2$). The scale coefficient is the probability of the stimulated transition $B_{\lambda,s}(E)$. Then the stimulated emission can be written as

$$\int_{E_1}^{E_2} B_{\lambda,s}(E)N_{sc}(E+h\nu)F_{sH}(E+h\nu)N_t(E)[1-F_{sL}(E)]dE$$

Therefore the recombination current J_{b1} can be expressed as

$$\begin{aligned} J_{b1} &= e\int_{E_1+h\nu}^{E_2+h\nu}\int_{E_1}^{E_2} A_s(E,E')N_{sc}(E)F_{sH}(E)N_t(E')[1-F_{sL}(E')]dE'dE \\ &+e\int_{E_1}^{E_2} B_{\lambda,s}(E)N_{sc}(E+h\nu)F_{sH}(E+h\nu)N_t(E)[1-F_{sL}(E)]dE \end{aligned} \tag{S2-8}$$

According to the principle of detailed balance, the influx rate should equal to the efflux rate of electrons on the coupled levels in the conduction band of the substrate, and thus the transmission current (ΔJ_1) of the electrons from the substrate to the coupled molecular levels can be expressed as

$$\Delta J_1 = J_{a1} - J_{b1} \tag{S2-9}$$

Since these electrons transfer to molecular orbital through resonant tunneling,[13, 14] ΔJ_1 can be written as

$$\Delta J_1 = T_{BW} J_{a1} \tag{S2-10}$$

where T_{BW} is the transmission coefficient and depends only on the energy of the electrons for given molecules and substrate system at low defect concentration. Using above equations, we can get

$$\begin{aligned} &\int_{E_1+h\nu}^{E_2+h\nu}\int_{E_1}^{E_2} A_s(E,E')N_{sc}(E)F_{sH}(E)N_t(E')[1-F_{sL}(E')]dE'dE \\ &+\int_{E_1}^{E_2} B_{\lambda,s}(E)N_{sc}(E+h\nu)F_{sH}(E+h\nu)N_t(E)[1-F_{sL}(E)]dE \\ &=\int_{E_1}^{E_2} [1-T_{BW}(E+h\nu)]B_{\lambda,s}(E)N_t(E)F_{sL}(E)N_{sc}(E+h\nu)[1-F_{sH}(E+h\nu)]dE \end{aligned} \tag{S2-11}$$

By replacing all the E_2 in integral upper limits for single integrals and E_2 in the integral upper limits in outer integrals for double integral with an independent variable x ($x\in[E_1,E_2]$), equation (S2-11) can be rewritten as

$$\begin{aligned}&\int_{E_1+h\nu}^{x+h\nu}\int_{E_1}^{E_2}A_s(E,E')N_{sc}(E)F_{sH}(E)N_t(E')\left[1-F_{sL}(E')\right]dE'dE\\&+\int_{E_1}^{x}B_{\lambda,s}(E)N_{sc}(E+h\nu)F_{sH}(E+h\nu)N_t(E)[1-F_{sL}(E)]dE\\&=\int_{E_1}^{x}[1-T_{BW}(E+h\nu)]B_{\lambda,s}(E)N_t(E)F_{sL}(E)N_{sc}(E+h\nu)[1-F_{sH}(E+h\nu)]dE\end{aligned}\tag{S2-12}$$

By calculating the derivative of equation (S2-12) with respect to x and using the mean value theorems for definite integrals, $F_{sH}(x+h\nu)$ can be calculated as

$$F_{sH}(x+h\nu)=\frac{[1-T_{BW}(x+h\nu)]B_{\lambda,s}(x)N_t(x)F_{sL}(x)}{A_s(x+h\nu,\xi_1)\left[1-F_{sL}(\xi_1)\right]M_t+[1-T_{BW}(x+h\nu)F_{sL}(x)]B_{\lambda,s}(x)N_t(x)}\tag{S2-13}$$

ξ_1 is a point in $[E_1,E_2]$. Substituting equation (S2-13) into equations (S2-7), (S2-8), (S2-9) and (S2-10), ΔJ_1 can be expressed as

$$\begin{aligned}&\Delta J_1=(G_1G_2/G_3)M_t\\&G_1=eT_{BW}(\xi_2+h\nu)B_{\lambda,s}(\xi_2)F_{sL}(\xi_2)N_{sc}(\xi_2+h\nu)\\&G_2=A_s(\xi_2+h\nu,\xi_1)\left[1-F_{sL}(\xi_1)\right](E_2-E_1)+B_{\lambda,s}(\xi_2)[1-F_{sL}(\xi_2)]\\&G_3=A_s(\xi_2+h\nu,\xi_1)\left[1-F_{sL}(\xi_1)\right](E_2-E_1)+[1-T_{BW}(\xi_2+h\nu)F_{sL}(\xi_2)]B_{\lambda,s}(\xi_2)\end{aligned}\tag{S2-14}$$

in which an approximate equation $M_t=(E_2-E_1)N_t(E)$ has been used as M_t is supposed to be very small, and thus $N_t(E)$ can be regarded evenly distributed from E_1 to E_2. ξ_2 is a point in $[E_1,E_2]$. And with a small M_t, the energy structure, lattice structure and adsorptivity of the substrate are invariant with the defect concentration, and therefore, $B_{\lambda,s}(E)$, $A_s(E,E')$, $N_{sc}(E)$, ξ_1 and ξ_2 are irrelevant with M_t and the difference in $F_{sL}(E)$ can be ignored, G_1, G_2 and G_3 are independent of M_t, and finally equation (S2-14) can be rewritten as

$$\Delta J_1=a\cdot M_t\tag{S2-15}$$

in which a is a constant determined by excitation light, temperature, the adsorbed molecules and the substrate. If $a>0$, ΔJ_1 linearly increases with M_t, and if $a<0$, there is no CT_1 process. Since the current injected onto molecular energy levels above the LUMO is proportional to the enhancement factor of all the vibration modes of the molecular SERS spectrum in the PICT, the intensity of SERS signals in CT_1 can be written as

$$I_1=a\cdot M_t\tag{S2-16}$$

The CT_2 process

When the photon energy is not high enough, i.e. $h\nu>E_{cm}-E_2$ but $h\nu<E_{LUMO}-E_2$ *and* $2h\nu>E_{LUMO}-E_2$, the CT_2 process takes place. After absorbing a photon, the electron on the defect levels will transit to the energy levels in the conduction band of the substrate that are not coupled with molecular levels above LUMO with the current of J_{a21}. If $F_{sM}(E+h\nu)$ is the electron distribution function on these uncoupled levels in the conduction band of the substrate ($E_1<E<E_2$), J_{a21} is proportional to the density of the filled initial levels $N_t(E)F_{sL}(E)$ and the density of the unfilled final levels $N_s(E+h\nu)[1-F_{sM}(E+h\nu)]$. The scale coefficient is the probability of the stimulated transition $B_{\lambda,s}(E)$. Therefore the transition current J_{a21} can be expressed as

$$J_{a21}=e\int_{E_1}^{E_2}B_{\lambda,s}(E)N_t(E)F_{sL}(E)N_s(E+h\nu)[1-F_{sM}(E+h\nu)]dE\tag{S2-17}$$

After excited to the transition levels, the electrons will be recombined through the spontaneous transition and the stimulated emission as mentioned above, the recombination current J_{b21} can be expressed as

$$\begin{aligned}J_{b21}=&e\int_{E_1+h\nu}^{E_2+h\nu}\int_{E_1}^{E_2}A_s(E,E')N_s(E)F_{sM}(E)N_t(E')\left[1-F_{sL}(E')\right]dE'dE\\&+e\int_{E_1}^{E_2}B_{\lambda,s}(E)N_s(E+h\nu)F_{sM}(E+h\nu)N_t(E)[1-F_{sL}(E)]dE\end{aligned}\tag{S2-18}$$

Electrons on the uncoupled levels can absorb another photon in a very short time, and transit to higher levels in the conduction band of the substrate coupled with molecular levels above LUMO with the current of J_{a22}. J_{a22} is

proportional to the density of the filled initial levels $N_s(E)[1\text{-}F_{sM}(E)]$ and the density of the unfilled final levels $N_{sc}(E+h\nu)[1\text{-}F_{sH}(E+h\nu)]$ ($E_1+h\nu<E<E_2+h\nu$). The scale coefficient is the probability of the stimulated transition $B_{\lambda,s}(E)$. Therefore, the transition current J_{a22} can be expressed as

$$J_{a22} = e\int_{E_1+h\nu}^{E_2+h\nu} B_{\lambda,s}(E)N_s(E)F_{sM}(E)N_{sc}(E+h\nu)[1-F_{sH}(E+h\nu)]dE \tag{S2-19}$$

Electrons on the coupled levels in the conduction band of the substrate can be recombined in the defect levels through spontaneous transition with the current of J_{b22} expressed by

$$J_{b22} = e\int_{E_1+2h\nu}^{E_2+2h\nu}\int_{E_1}^{E_2} A_s(E,E')N_{sc}(E)F_{sH}(E)N_t(E')\left[1-F_{sL}(E')\right]dE'dE \tag{S2-20}$$

and through the stimulated emission to the lower level with energy difference of $h\nu$ in the uncoupled levels with the current of J_{b23} expressed by

$$J_{b23} = e\int_{E_1+h\nu}^{E_2+h\nu} B_{\lambda,s}(E)N_{sc}(E+h\nu)F_{sH}(E+h\nu)N_s(E)[1-F_{sM}(E)]dE \tag{S2-21}$$

According to the principle of detailed balance, the transmission current (ΔJ_2) of the electrons from the substrate to the coupled molecular levels above the LUMO thus can be expressed as

$$\Delta J_2 = J_{a22} - J_{b22} - J_{b23} \tag{S2-22}$$

or as

$$\Delta J_2 = T_{BW}J_{a22} \tag{S2-23}$$

Using equations (S2-19), (S2-20), (S2-21), (S2-22) and (S2-23), we can get

$$\begin{aligned}&\int_{E_1+h\nu}^{E_2+h\nu}[1-T_{BW}(E+h\nu)]B_{\lambda,s}(E)N_s(E)F_{sM}(E)N_{sc}(E+h\nu)[1-F_{sH}(E+h\nu)]dE\\&=\int_{E_1+2h\nu}^{E_2+2h\nu}\int_{E_1}^{E_2} A_s(E,E')N_{sc}(E)F_{sH}(E)N_t(E')\left[1-F_{sL}(E')\right]dE'dE\\&+\int_{E_1+h\nu}^{E_2+h\nu} B_{\lambda,s}(E)N_{sc}(E+h\nu)F_{sH}(E+h\nu)N_s(E)[1-F_{sM}(E)]dE\end{aligned} \tag{S2-24}$$

By using the same treatment as equation (S2-12) and (S2-13), we can get

$$\begin{aligned}&[1-T_{BW}(x+2h\nu)]B_{\lambda,s}(x+h\nu)N_s(x+h\nu)F_{sM}(x+h\nu)N_{sc}(x+2h\nu)[1-F_{sH}(x+2h\nu)]\\&=A_s(x+2h\nu,\xi_3)N_{sc}(x+2h\nu)F_{sH}(x+2h\nu)\left[1-F_{sL}(\xi_3)\right]M_t\\&+B_{\lambda,s}(x+h\nu)N_{sc}(x+2h\nu)F_{sH}(x+2h\nu)N_s(x+h\nu)[1-F_{sM}(x+h\nu)]\end{aligned} \tag{S2-25}$$

in which ξ_3 is a point in $[E_1,E_2]$. From the principle of detailed balance we know

$$J_{a21} + J_{b23} - J_{b21} - J_{a22} = 0 \tag{S2-26}$$

Substituting equations (S2-17), (S2-18), (S2-19), (S2-21) into equation (S2-26), one can get

$$\begin{aligned}&\int_{E_1}^{E_2} B_{\lambda,s}(E)N_t(E)F_{sL}(E)N_s(E+h\nu)[1-F_{sM}(E+h\nu)]dE+\int_{E_1+h\nu}^{E_2+h\nu} B_{\lambda,s}(E)N_{sc}(E+h\nu)F_{sH}(E+h\nu)N_s(E)[1-F_{sM}(E)]dE\\&-\int_{E_1+h\nu}^{E_2+h\nu}\int_{E_1}^{E_2} A_s(E,E')N_s(E)F_{sM}(E)N_t(E')\left[1-F_{sL}(E')\right]dE'dE-\int_{E_1}^{E_2} B_{\lambda,s}(E)N_s(E+h\nu)F_{sM}(E+h\nu)N_t(E)[1-F_{sL}(E)]dE\\&-\int_{E_1+h\nu}^{E_2+h\nu} B_{\lambda,s}(E)N_s(E)F_{sM}(E)N_{sc}(E+h\nu)[1-F_{sH}(E+h\nu)]dE=0\end{aligned} \tag{S2-27}$$

Here again by using the same treatment as equations (S2-12) and (S2-13), we can get

$$\begin{aligned}&B_{\lambda,s}(x)F_{sL}(x)[1-F_{sM}(x+h\nu)]N_t(x)+B_{\lambda,s}(x+h\nu)N_{sc}(x+2h\nu)[1-F_{sM}(x+h\nu)]F_{sH}(x+2h\nu)\\&-A_s(x+h\nu,\xi_4)\left[1-F_{sL}(\xi_4)\right]F_{sM}(x+h\nu)M_t-B_{\lambda,s}(x)[1-F_{sL}(x)]F_{sM}(x+h\nu)N_t(x)\\&-B_{\lambda,s}(x+h\nu)N_{sc}(x+2h\nu)F_{sM}(x+h\nu)[1-F_{sH}(x+2h\nu)]=0\end{aligned} \tag{S2-28}$$

in which ξ_4 is a point in $[E_1,E_2]$. Substituting equation (S2-25) into equation (S2-28), using the mean value theorems for definite integrals, $F_{sM}(x+h\nu)$ and $F_{sH}(x+2h\nu)$ can be calculated as

$$F_{sM}(x+h\nu)=\frac{G_4(x)M_t^{\,2}+G_5(x)N_t(x)M_t+[G_6(x)+G_7(x)]M_t+[G_8(x)+G_9(x)]N_t(x)+G_{10}(x)\pm\sqrt{\Delta_1(x)}}{2G_{11}(x)M_t+2G_{12}(x)N_t(x)+2G_{10}(x)} \tag{S2-29}$$

$$\begin{aligned}
G_4(x)&=A_s(x+h\nu,\xi_4)A_s(x+2h\nu,\xi_3)\left[1-F_{sL}(\xi_3)\right]\left[1-F_{sL}(\xi_4)\right]\\
G_5(x)&=A_s(x+2h\nu,\xi_3)B_{\lambda,s}(x)\left[1-F_{sL}(\xi_3)\right]\\
G_6(x)&=A_s(x+2h\nu,\xi_3)B_{\lambda,s}(x+h\nu)N_{sc}(x+2h\nu)\left[1-F_{sL}(\xi_3)\right]\\
G_7(x)&=A_s(x+h\nu,\xi_4)B_{\lambda,s}(x+h\nu)N_s(x+h\nu)\left[1-F_{sL}(\xi_4)\right]\\
G_8(x)&=B_{\lambda,s}(x)B_{\lambda,s}(x+h\nu)N_s(x+h\nu)\\
G_9(x)&=B_{\lambda,s}(x)B_{\lambda,s}(x+h\nu)N_s(x+h\nu)F_{sL}(x)T_{BW}(x+2h\nu)\\
G_{10}(x)&=B_{\lambda,s}{}^2(x+h\nu)N_s(x+h\nu)N_{sc}(x+2h\nu)T_{BW}(x+2h\nu)\\
G_{11}(x)&=A_s(x+h\nu,\xi_4)B_{\lambda,s}(x+h\nu)N_s(x+h\nu)\left[1-F_{sL}(\xi_4)\right]T_{BW}(x+2h\nu)\\
G_{12}(x)&=B_{\lambda,s}(x)B_{\lambda,s}(x+h\nu)N_s(x+h\nu)T_{BW}(x+2h\nu)
\end{aligned}$$

$$F_{sH}(x+2h\nu)=\frac{[G_{13}(x)-G_{14}(x)]F_{sM}(x+h\nu)}{G_{15}(x)M_t-G_{14}(x)F_{sM}(x+h\nu)+G_{13}(x)} \tag{S2-30}$$

$$\begin{aligned}
G_{13}(x)&=B_{\lambda,s}(x+h\nu)N_s(x+h\nu)\\
G_{14}(x)&=B_{\lambda,s}(x+h\nu)N_s(x+h\nu)T_{BW}(x+2h\nu)\\
G_{15}(x)&=A_s(x+2h\nu,\xi_3)\left[1-F_{sL}(\xi_3)\right]\\
G_{16}(x)&=B_{\lambda,s}(x)B_{\lambda,s}(x+h\nu)N_s(x+h\nu)F_{sL}(x)
\end{aligned}$$

$$\begin{aligned}
\Delta_1(x)&=[G_4(x)M_t^{\,2}+G_5(x)N_t(x)M_t]^2\\
&+2[G_4(x)G_{17}(x)M_t^{\,2}+G_{18}(x)N_t(x)M_t+G_5(x)G_{19}(x)N_t^{\,2}(x)]M_t\\
&+[G_{20}(x)M_t^{\,2}+2G_{21}(x)N_t(x)M_t+G_{19}^{\,2}(x)N_t^{\,2}(x)]\\
&+2G_{10}(x)[G_{17}(x)M_t+G_{22}(x)N_t(x)]\\
&+G_{10}^{\,2}(x)
\end{aligned} \tag{S2-31}$$

$$\begin{aligned}
G_{17}(x)&=G_6(x)+G_7(x)\\
G_{18}(x)&=G_5(x)G_6(x)+2G_4(x)G_8(x)-G_4(x)G_9(x)\\
G_{19}(x)&=G_8(x)-G_9(x)\\
G_{20}(x)&=[G_6(x)+G_7(x)]^2+2G_6(x)G_{11}(x)\\
G_{21}(x)&=G_{17}(x)G_{19}(x)+G_6(x)G_{12}(x)\\
G_{22}(x)&=G_8(x)+G_9(x)-2G_{16}(x)
\end{aligned}$$

Substituting equations (S2-19), (S2-29), (S2-30) and (S2-31) into equation (S2-23), using the mean value theorem for definite integrals and an approximate equation of $M_t=(E_2-E_1)N_t(E)$, ΔJ_2 can be obtained as

$$\Delta J_2=eG_{23}\frac{G_{24}M_t^{\,2}+G_{25}M_t+G_{27}\pm\sqrt{\Delta_2(M_t)}}{G_{26}M_t+2G_{27}}K(M_t) \tag{S2-32}$$

in which

$$K(M_t)=\frac{1-P(M_t)}{1-T_{BW}(\xi_5+2h\nu)P(M_t)} \tag{S2-33}$$

$$P(M_t)=G_{29}\frac{G_{24}M_t^{\,2}+G_{25}M_t+G_{27}\pm\sqrt{\Delta_2(M_t)}}{(G_{28}M_t+G_{29})(G_{26}M_t+2G_{27})} \tag{S2-34}$$

$$\Delta_2(M_t)=G_{24}^{\,2}M_t^4+G_{30}M_t^3+G_{31}M_t^2+G_{32}M_t+G_{27}^{\,2} \tag{S2-35}$$

$$G_{23} = B_{\lambda,s}(\xi_5 + h\nu)N_s(\xi_5 + h\nu)N_{sc}(\xi_5 + 2h\nu)T_{BW}(\xi_5 + 2h\nu)$$
$$G_{24} = G_4(\xi_5) + \frac{G_5(\xi_5)}{E_2 - E_1}$$
$$G_{25} = G_6(\xi_5) + G_7(\xi_5) + \frac{G_8(\xi_5) + G_9(\xi_5)}{E_2 - E_1}$$
$$G_{26} = 2[G_{11}(\xi_5) + \frac{G_{12}(\xi_5)}{E_2 - E_1}]$$
$$G_{27} = G_{10}(\xi_5)$$
$$G_{28} = G_{15}(\xi_5)$$
$$G_{29} = G_{13}(\xi_5)$$
$$G_{30} = 2[G_4(\xi_5)G_{17}(\xi_5) + \frac{G_{18}(\xi_5)}{E_2 - E_1} + \frac{G_5(\xi_5)G_{19}(\xi_5)}{(E_2 - E_1)^2}]$$
$$G_{31} = G_{20}(\xi_5) + \frac{2G_{21}(\xi_5)}{E_2 - E_1} + \frac{G_{19}^2(\xi_5)}{(E_2 - E_1)^2}$$
$$G_{32} = 2G_{10}(\xi_5)[G_{17}(\xi_5) + \frac{G_{22}(\xi_5)}{E_2 - E_1}]$$

The choice of "±" in equation (S2-34) is the same with the choice in equation (S2-32). ζ_5 is a point in $[E_1,E_2]$ and is irrelevant with M_t. All the physical quantities are constants determined by excitation light, temperature, the adsorbed molecules and the substrate except M_t, and therefore ΔJ_2 is also dependent only on M_t. Ignoring the non-integral power as they can be roughly simulated by adjacent integer power within finite interval, ΔR_2 can be expressed as

$$\Delta J_2 = \frac{M_t^4 + a_1 M_t^3 + a_2 M_t^2 + a_3 M_t + a_4}{b_1 M_t^3 + b_2 M_t^2 + b_3 M_t + b_4} \tag{S2-36}$$

where a_i and b_i (i=1, 2, 3, 4) are constants irrelevant with M_t. There are totally 8 undetermined coefficients in equation (S2-36), and since the exact coefficients is meaningless, our attention focuses on the variation tendency of ΔJ_2 with M_t, and further simplification is acceptable.

Equation (S2-35) can be rewritten as

$$\Delta_2(M_t) = (G_{24}M_t^2 + G_{33}M_t + G_{27})^2 - 2G_{36}M_t^3 - G_{34}M_t^2 - 2G_{35}M_t \tag{S2-37}$$

$$G_{33} = G_{17}(\xi_5) + \frac{G_8(\xi_5)}{E_2 - E_1}$$
$$G_{34} = G_9(\xi_5)[2\frac{G_{17}(\xi_5)}{E_2 - E_1} + \frac{2G_8(\xi_5) - G_9(\xi_5)}{(E_2 - E_1)^2}]$$
$$G_{35} = G_{10}(\xi_5)\frac{2G_{16}(\xi_5) - G_9(\xi_5)}{E_2 - E_1}$$
$$G_{36} = \frac{G_9(\xi_5)}{E_2 - E_1}G_{24}$$

Since G_i are all positive numbers, and from equation (S2-37) we get

$$\sqrt{\Delta_2(M_t)} < G_{24}M_t^2 + G_{33}M_t + G_{27} \tag{S2-38}$$

From equations (S2-38) and (S2-34) we have $P(M_t)>0$ whether taking "+" or "-" in "±". Since $\Delta J_2>0$, and from equation (S2-33) we have $P(M_t)<1$. As the transmission coefficient $T_{BW}(\xi_5+2h\nu)$ is always less than 1, and therefore we have $0<K(M_t)<1$. The $K(M_t)$ value is either about zero or about 1 from the calculation of equation (S2-33) when either taking "+" or "-" in "±" of the equation when M_t is very small. In either case $K(M_t)$ can be considered as a constant k. And equation (S2-32) can be rewritten as

$$\Delta J_2 = ekG_{23}\frac{G_{24}M_t^{\,2} + G_{25}M_t + G_{27} \pm \sqrt{\Delta_2(M_t)}}{G_{26}M_t + 2G_{27}} \tag{S2-39}$$

and finally in the form

$$\Delta J_2 = \frac{M_t^{\,2} + a_1 M_t + a_2}{b_1 M_t + b_2} \tag{S2-40}$$

where a_i and b_i (i=1,2) are all constants irrelevant with M_t. The intensity of SERS signals in CT_2 can be written as

$$I_2 = \frac{M_t^2 + a_1 M_t + a_2}{b_1 M_t + b_2} \tag{S2-41}$$

2) Applications

For the molecules whose LUMO or HOMO are pinned to the Fermi level of the substrate, introducing defect will change the Fermi level, resulting in the change in the molecular energy levels relatively to the substrate, which in turn will change the pattern of the PICT process. Therefore there will exist several stages in the PICT process, and each stage contains different sub-PICT processes. For the molecules whose HOMO is pinned under the Fermi level of the substrate

$$E_{HOMO} = E_{CM} - h(x) - 0.3eV \tag{S2-42}$$

$$E_{LUMO} = E_{CM} - h(x) - 0.3eV + (E_{LUMO} - E_{HOMO}) \tag{S2-43}$$

For the molecules whose LUMO is pinned above the Fermi level of the substrate

$$E_{HOMO} = E_{CM} - h(x) + 0.1eV - (E_{LUMO} - E_{HOMO}) \tag{S2-44}$$

$$E_{LUMO} = E_{CM} - h(x) + 0.1eV \tag{S2-45}$$

where E_F and E_{CM} are respectively the Fermi level and the bottom of conduction band of substrate, $h(x)$ is the energy difference between the upper conduction band minimum and the Fermi level at the non-stoichiometry, x, of the substrate. E_{LUMO}-E_{HOMO} is the energy difference between the LUMO and the HOMO of the molecules, and is a constant.

Take oxygen vacancy as an example of the defect energy levels. For α-MoO_{3-x} nanobelts, $h(x)$ can be obtained from the data in reference,[15] as shown in Fig. S1, and after fitting we get

$$h(x) = 0.184 - 0.016ln(x + 3.12\times10^{-5}) \tag{S2-46}$$

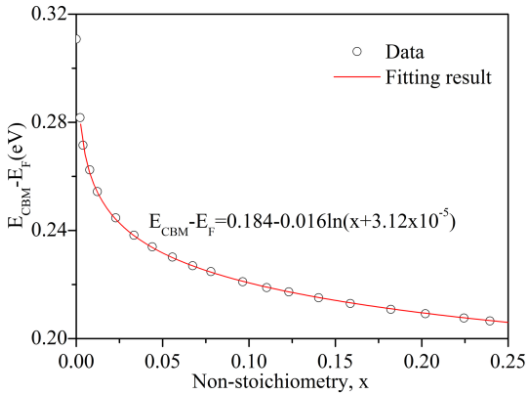

Fig. S1 Plot of Fermi-level position (relative to the conduction band minimum, E_{CBM}) as a function of nonstoichiometry x in α-MoO_{3-x} nanobelts.

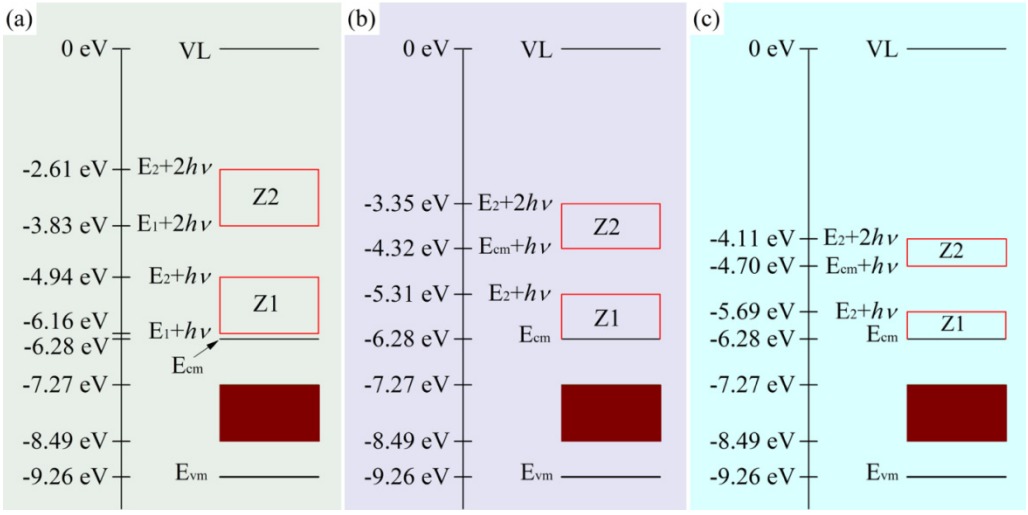

Scheme S4. Energy diagrams of MoO_{3-x} nanobelts excited with laser wavelength of (a) 532 (2.33 eV), (b) 633 (1.96 eV) and (c) 785 nm (1.58 eV). Z_1 and Z_2 are the energy levels zone involved in the CT_1 and CT_2 process, respectively.

(1) The 614 cm^{-1} characteristic peak of R6G on α-MoO_{3-x} nanobelts with 532 nm laser

In the first stage (0<x<0.02631), since the HOMO of R6G is pinned under the Fermi level of MoO_{3-x} nanobelts, E_{LUMO} of R6G will increase with the increased E_F in α-MoO_{3-x} nanobelts due to the increase in x value. The change in the E_2 value can be ignored and only the defect levels with the energy in $[E_{LUMO}\text{-}h\nu\text{-}\gamma, E_2]$ is involved in CT_1, thus the defect levels involved in the CT_1 decreases with the increasing E_{LUMO} originated from the increasing x value. The value of γ (the largest energy difference of two coupled levels between α-MoO_{3-x} nanobelts and R6G) can be obtained by analyzing experimental results. One can find that the Raman intensity of R6G on α-MoO_{3-x} nanobelts with x<0.02631 is much stronger than that with x>0.02631. This result indicates that when x<0.02631, the CT_1 exists in the PICT between α-MoO_{3-x} nanobelts and R6G, thus CT_2 can be ignored. When x>0.02631, CT_1 disappears and CT_2 dominants the PICT process. Substituting x=0.02631 into equation (S2-46), we get $h(0.02631)$= 0.24 eV, indicating the E_F of α-MoO_{3-x} nanobelts (x=0.02631) is at -6.52 eV (see Scheme S5). And thus γ~0.42 eV, implying that the energy level between α-MoO_{3-x} nanobelts and R6G with the energy difference less than 0.42 eV can be coupled. Since the critical x value could be between 0.02631 and 0.03219, the real γ value may be slight higher than 0.42 eV.

A function factor $\varphi(x)$ can be introduced into $I=ax+153$ to describe the defect levels involved in CT_1 with different x values,

$$I = a\phi(x)x + 153 \tag{S2-47}$$

Precisely speaking, the difference between the higher defect levels and the lower defect levels will affect the density of states, electron distribution functions and transition probability. Since the energy difference in E_F from x=0 to x=0.02631 is very small (~0.11 eV), the defect levels involved in CT_1 is only a very small proportion among all the defect levels (~1.2 eV).[15] Therefore, the difference of the physical quantities in the defect levels can be ignored, and thus $\varphi(x)$ can be written as

$$\phi(x) = \frac{E_2 - [E_{LUMO}(x) - h\nu - \gamma]}{E_2 - [E_{LUMO}(0) - h\nu - \gamma]} \tag{S2-48}$$

Substituting equations (S2-43) and (S2-46) into equation (S2-48), $\varphi(x)$ can be rewritten as

$$\phi(x) = \frac{E_2 - [E_{CBM} - h(x) - 0.3eV + (E_{LUMO} - E_{HOMO}) - h\nu - \gamma]}{E_2 - [E_{CBM} - h(0) - 0.3eV + (E_{LUMO} - E_{HOMO}) - h\nu - \gamma]} \tag{S2-49}$$

in which $0 \le x \le 0.02631$. Using E_2=-7.27eV, E_{CBM}=-6.28eV, $h(x)$=0.184-0.016ln(x+3.12×10^{-5}), E_{LUMO}-E_{HOMO}=2.3

eV， $h\nu$=2.33eV and γ=0.42eV, finally $\varphi(x)$ can be obtained as

$$\phi(x) = -0.145ln\left(x + 3.12\times10^{-5}\right) - 0.509 \quad \text{(S2-50)}$$

Substituting equation (S2-50) into equation (S2-47) we get

$$I = -a[0.145ln\left(x + 3.12\times10^{-5}\right) + 0.509]x + 153 \quad \text{(S2-51)}$$

where a is a positive constant, $0 \le x \le 0.02631$. If sets $a=3.546\times10^7$, the experimental date can fit equation (S2-51) very well. Therefore, the Raman intensity of the characteristic Raman peak at 614 cm^{-1} of R6G on α-MoO_{3-x} nanobelts excited with 532 nm laser can be expressed as

$$I = (3.546\times10^7 x)[-0.145ln(x + 3.12\times10^{-5}) - 0.509] + 153 \quad (0 \le x \le 0.02631) \quad \text{(S2-52)}$$

see the red dashed line in Fig. 4 (a).

At stage II ($0.02631 < x < 0.05387$), φ(x)=1(φ(x) is a piecewise function of x), and the Raman intensity of the characteristic Raman peak can be expressed as

$$I = \frac{x^2 + a_1 x + a_2}{b_1 x + b_2} + 153 \quad \text{(S2-53)}$$

where a_i and b_i (i=1, 2) are constants. It also can well-fit the experimental data with appropriate values of a_i and b_i (the olive dashed line in Fig. 4 (a)), and finally I can be expressed as

$$I = \frac{x^2 - 0.083x + 2.269\times10^{-3}}{2.659\times10^{-5}x - 6.435\times10^{-7}} + 153 \quad \text{(S2-54)}$$

In the third stage (x>0.05387), I=153 and is a constant.

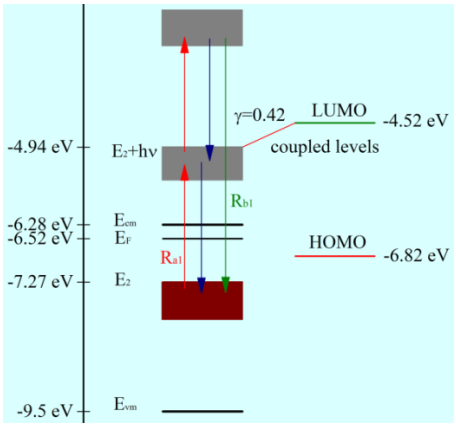

Scheme S5. Energy diagrams of R6G and α-MoO_{3-x} nanobelts with x=0.02631 excited with 532 nm laser.

(2) The 608 cm^{-1} characteristic peak of R6G on α-MoO_{3-x} nanobelts with 633 nm laser

This situation is similar with stage II of R6G on α-MoO_{3-x} nanobelts with 532 nm laser. The only difference is a decreased photon energy. In this case, CT_3 disappears and only CT_2 exists. All the defect levels will be involved (Scheme S4b), φ(x)=1, and the intensity can be written as

$$I = \frac{x^2 + a_1 x + a_2}{b_1 x + b_2} \quad \text{(S2-55)}$$

till x=0.02544, see Fig. 4b When x>0.02544, all the excited electrons in MoO_{3-x} nanobelts will be recombined and the PICT disappears. After fitting with experimental date (Fig. 4b), the relationship between I and x when x<0.02544can be written as

$$I = \frac{x^2 + 4.425\times10^{-3}x - 7.598\times10^{-4}}{-2.823\times10^{-4}x - 2.434\times10^{-6}} \quad \text{(S2-56)}$$

(3) The 1595 cm^{-1} characteristic peak of 4-MBA on α-MoO_{3-x} nanobelts with 532 nm laser

For 4-MBA, E_{LUMO} = -3.85eV and E_{HOMO} = -8.48eV, the PICT process contains only CT_2. Considering the γ (about 0.26 eV), all defect levels will be involved (Scheme S4a) and the molecular levels of 4-MBA is not pinned to E_F, thus the function factor $\varphi(x)$ is not needed. The relationship between the intensity and the non-stoichiometry when x<0.02544 can be written as

$$I = \frac{x^2 + a_1 x + a_2}{b_1 x + b_2} \tag{S2-57}$$

After fitting with experimental date (Fig. 4c), above equation can be rewritten as

$$I = \frac{x^2 + 0.158x - 4.676\times10^{-3}}{-1.870\times10^{-4}x - 4.007\times10^{-6}} \tag{S2-58}$$

If x>0.02544, the efficiency of CT_2 drops to zero and the PICT disappears, and thus no SERS effect can be observed.

(4) The 1624 cm^{-1}characteristic peak of MB on α-MoO_{3-x} nanobelts with 532 nm laser

The PICT process contains CT_1, CT_2 and CT_3 and can be divided into three stages. At the first stage ($0<x<0.02631$), CT_1 and CT_3 constitute the PICT process and

$$I = a\varphi(x)x + b \tag{S2-59}$$

in which $\varphi(x)$=-0.16-0.046ln(x+0.0000312) and b=1896. γ=-0.07eV (Scheme S6). a is the only fitting constant and if sets as 5.266×10^7, the equation (S2-59) can fit experimental data very well, see the red dashed line in Fig. 4d. Therefore, the relationship between intensity I and x can be rewritten as

$$I = (5.266\times10^7 x)[-0.046\ln(x + 3.12\times10^{-5}) - 0.16] + 1896 \tag{S2-60}$$

In the second stage ($0.02631<x<0.05387$), CT_1 disappears and the PICT process contains CT_2 and CT_3 (Scheme S6). Obviously all the defect levels will be involved in CT_2 (φ(x)=1), and the peak intensity can be written as

$$I = \frac{x^2 + a_1 x + a_2}{b_1 x + b_2} + 1896 \tag{S2-61}$$

where a_i and b_i (i=1, 2) are constants and can be got from fitting with experimental data, the fitting result gives

$$I = \frac{x^2 - 0.078x + 1.270\times10^{-3}}{-4.735\times10^{-6}x + 1.157\times10^{-7}} + 1896 \tag{S2-62}$$

see the olive dashed line in Fig. 4d. At the third stage (x>0.05387), the CT_2 disappears and only CT_3 exists, the peak intensity is constant and can be written as I=1896 (black dashed line in Fig. 4d).

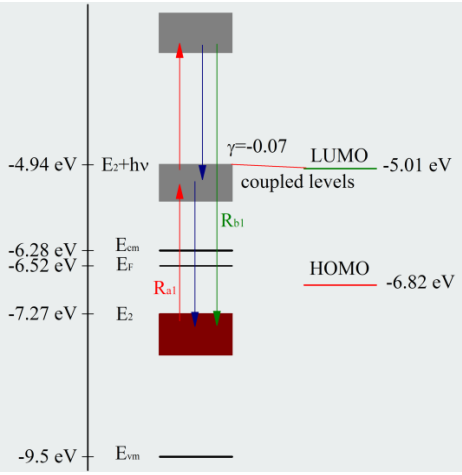

Scheme S6. Energy diagrams of MB and α-MoO_{3-x} nanobelts with x=0.02631 excited with 532 nm laser.

(5) The 1626 cm^{-1} characteristic peak of MB on α-MoO_{3-x} nanobelts with 633 nm laser

For MB on α-MoO_{3-x} with 633 nm laser, the PICT contains both CT_2 and CT_3 instead of CT_1 and CT_3 as predict from our model shows Table 2, due to the realignment of energy levels considering the change in Fermi level (calculated using $E_{LUMO}=E_{CM}-h(x)+(E_{LUMO}-E_{HOMO})-0.3eV$)). When $x<0.02631$, all the defect levels are involved in the CT_2 ($\varphi(x)=1$) and the intensity can be written as

$$I=\frac{x^2+a_1x+a_2}{b_1x+b_2}+2877 \tag{S2-63}$$

which fits the experimental data quite well (the olive line in Fig. 4e), and from the fitting result we get

$$I=\frac{x^2-0.010x-4.741\times10^{-4}}{2.466\times10^{-6}x-8.572\times10^{-8}}+2877 \tag{S2-64}$$

When $x>0.02631$, there exist only CT_3, $I=2877$ (black dashed line in Fig. 4e).

(6) The 1622 cm^{-1}characteristic peak of MB on α-MoO_{3-x} nanobelts with 785 nm laser

In this case, only CT_2 exists and all the defect levels are involved ($\varphi(x)=1$). The intensity can be expressed as

$$I=\frac{x^2+a_1x+a_2}{b_1x+b_2}. \tag{S2-65}$$

After fitting with experimental date (Fig. 4f), we get

$$I=\frac{x^2-0.259x+0.019}{1.146\times10^{-5}x+6.800\times10^{-7}} \tag{S2-66}$$

3. Crystal and band structure of α-MoO_3

α-MoO_3 is thermodynamically stable crystallizes with a unique orthorhombic crystal structure (space group Pbnm),[16, 17] and the lattice constant: a=3.962 Å, b=13.855 Å, c=3.699 Å. The crystal structure of α-MoO_3 consists of a series of bilayer with two distorted MoO_6 octahedra sublayers (Fig. S2) There are three crystallographically inequivalent oxygen sites, namely O(1), O(2) and O(3), as shown in Fig. S2b. Singly coordinated (terminal) oxygen O(1) is bonded to only one Mo atom by a very short Mo-O bond length of 1.67 Å. Two-coordinate oxygen O(2) is bonded to two neighboring Mo atoms asymmetrically in a sublayer with a bond length of 1.73 and 2.25 Å. Three-coordinate oxygen O(3) is bonded to two neighboring Mo atoms symmetrically in a sublayer with a bond length of 1.94 Å and a neighboring Mo atom in the other sublayer with a bond length of 2.33 Å. The interaction between each bilayer in the [010] direction is mainly a weak van der Waals. α-MoO_3 tends to grow along [001] direction owning to its layered structure and different bonding situations between [100] and [001] directions.[18, 19]

α-MoO_3 is a $4d^0$ Mo(VI) insulator with a bandgap of ca. 3.2 eV (single crystalline) and work function of ca. 7.8V (calculated through Mulliken electronegativity).[15, 17, 20] The valence band is dominated by O 2p states with only a very minor contribution from Mo states, and the conduction band is dominated by Mo d states with some hybridization with O 2p states, which consistent with the general feature of the electronic structure of wide band gap binary d^0 oxides.[17]

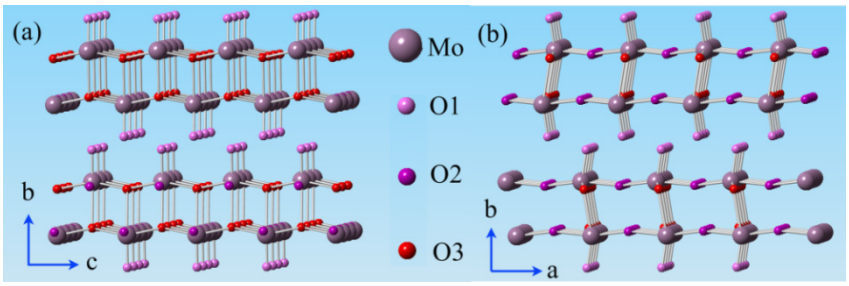

Fig. S2 Crystal structure of α-MoO_3 viewed along the axe of (a) [100] and (b) [001].

4. Preparation and characterization of α-MoO_3 samples

Nine α-MoO_3 samples were prepared. Number one is micro-sized α-MoO_3 particles (α-MoO_3 MPs) and number 2-9 are α-MoO_3 nanobelts. After hydrothermal synthesis, annealing treatment of nanobelts was performed under different conditions to induce different oxygen vacancy concentrations in α-MoO_3 nanobelts,[17] as shown in Table S1.

Table S1. Preparation condition and x value of α-MoO_{3-x} nanobelts calculated from XPS results

MoO_{3-x} nanobelts	Preparation condition	x value
a	annealing at 773K in air for 1 h (A)	~0
b	drying at 353 K in vacuum for 12 h (B)	0.00337
c	A + annealing at 473 K in vacuum for 1 h	0.01851
d	B + annealing at 473 K in vacuum for 1 h	0.02544
e	A + annealing at 573 K in vacuum for 1 h	0.02631
f	A + annealing at 673 K in vacuum for 1 h	0.03219
g	B + annealing at 573 K in vacuum for 1 h	0.05387
h	B + annealing at 673 K in vacuum for 1 h	0.1768

XRD analysis confirmed that all the samples are pure α-MoO_3, as shown in Fig. S3. FESEM observations show that α-MoO_3 MPs have an average size of several hundred microns, as shown in Fig. S4a, while the α-MoO_3 nanobelts with several tens of micrometers in length, about 200 nm in width, and about 20 nm in thickness, as shown in Fig. S4b. TEM observation and the corresponding HRTEM analysis indicate that the nanobelts grow along [200] direction with exposed (010) plane, as shown in Fig. S4c. The non-stoichiometry, x, in α-MoO_{3-x} nanobelts was calculated from XPS analysis, as shown in Fig. S5, and the results are also shown in Table S1.

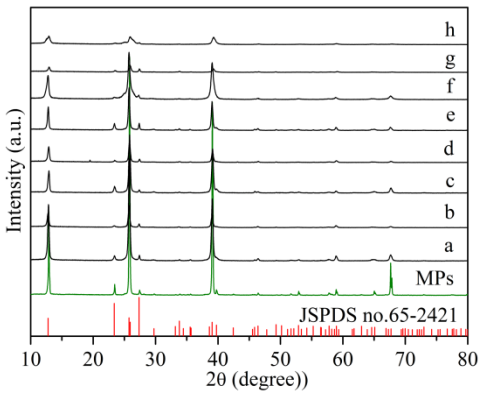

Fig. S3 XRD pattern of α-MoO_3 MPs and α-MoO_{3-x} nanobelts together with that from standard α-MoO_3 (JSPDS card no. 65-2421).

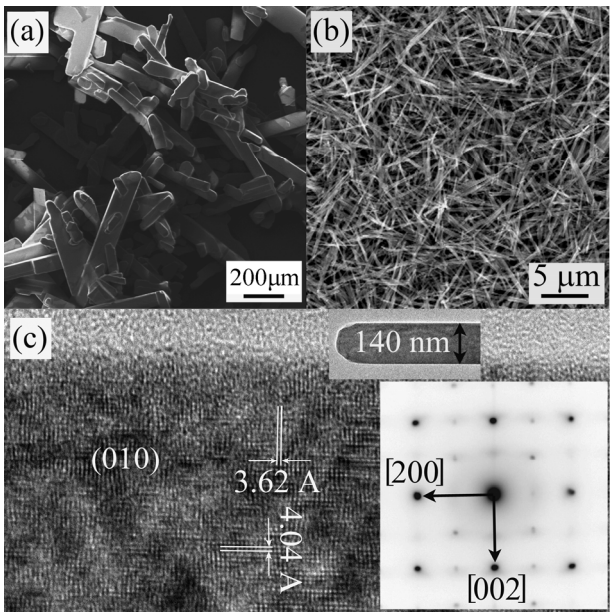

Fig. S4 FESEM images of (a) α-MoO_3 micro-sized particles and (b) α-MoO_{3-x} nanobelts. (c) TEM image (top inset) and the corresponding HRTEM image and SAED pattern (down inset) of α-MoO_{3-x} nanobelts.

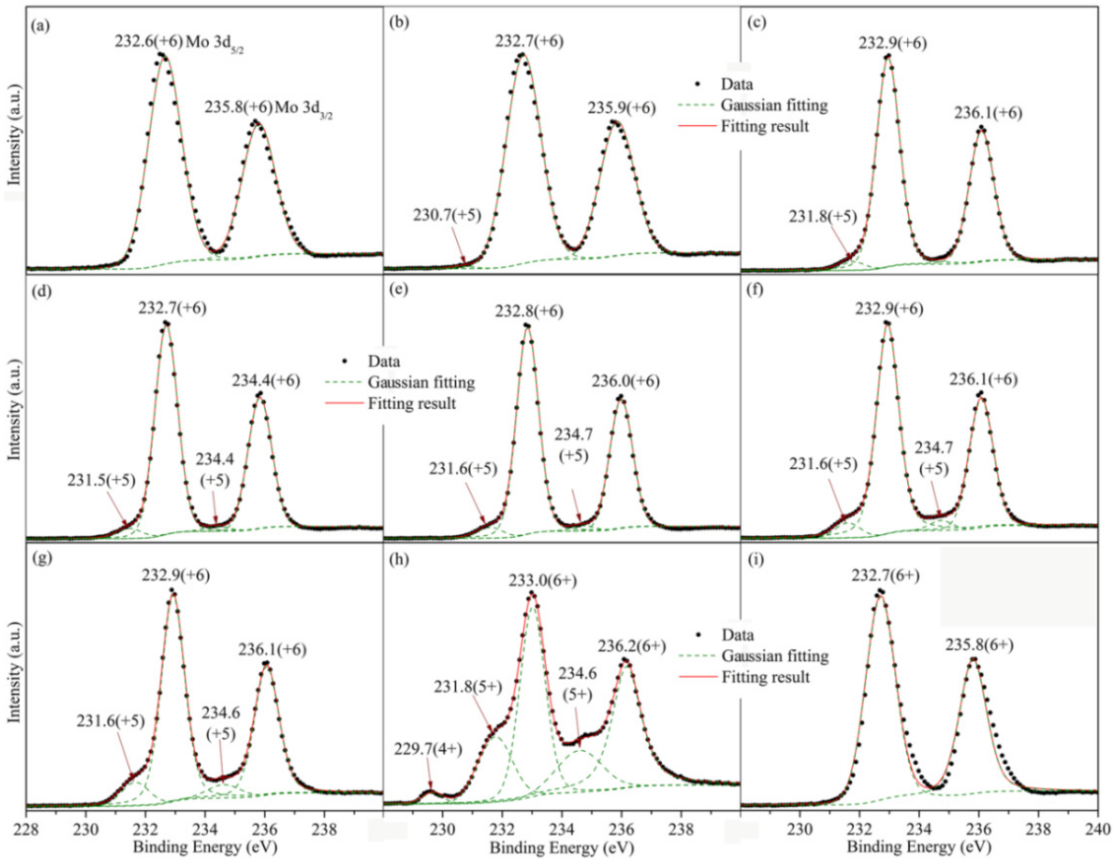

Fig. S5 XPS spectra of Mo 3d and the corresponding Gaussian fittings of (a-h) α-MoO_{3-x} nanobelts and (i) α-MoO_3 MPs. The peak components for Mo^{6+} and Mo^{5+} are indicated.

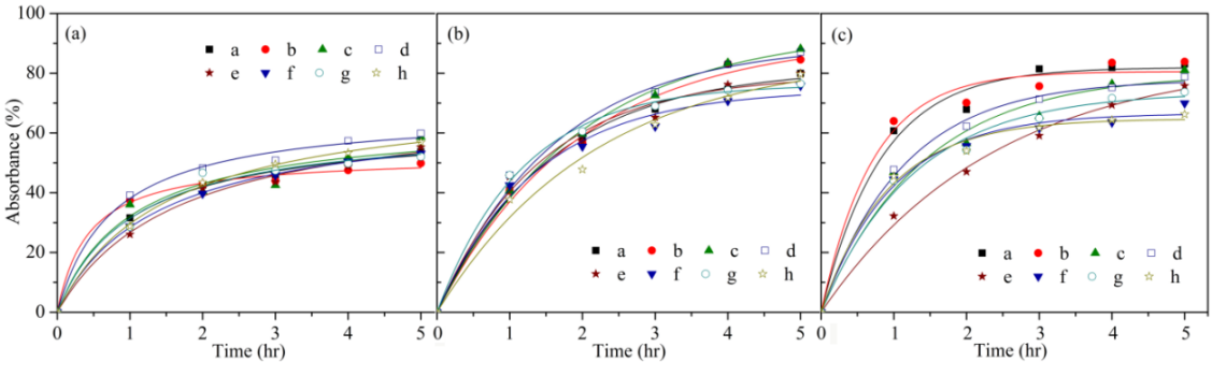

Fig. S6 Time evolution of chemisorption of (a) 4-MBA (10^{-4} M) and physisorption of (b) MB (10^{-5} M) and (c) R6G (10^{-5} M) on α-MoO_{3-x} nanobelt samples (sample a-h) (1mg/10ml).

Fig. S6 shows adsorbance of 4-MBA, MB and R6G on α-MoO_3 nanobelts with different oxygen vacancy concentrations. The adsorbance of R6G and MB can be fitted by following equation (physisorption),

$$q_t = q_e(1 - e^{-k_1 t}) \tag{S4-1}$$

while adsorbance of 4-MBA can be fitted by following equation (chemisorption),

$$\frac{t}{q_t} = \frac{1}{k_2 q_e^2} + \frac{t}{q_e} \tag{S4-2}$$

where q_t is the adsorbance at time t, q_e is the fitted value of the adsorbance at equilibrium, k_1 and k_2 are rate constants. From Fig. S6 one can see that the difference in adsorbance of different nanobelt samples is very small and therefore the influence on SERS can be ignored.

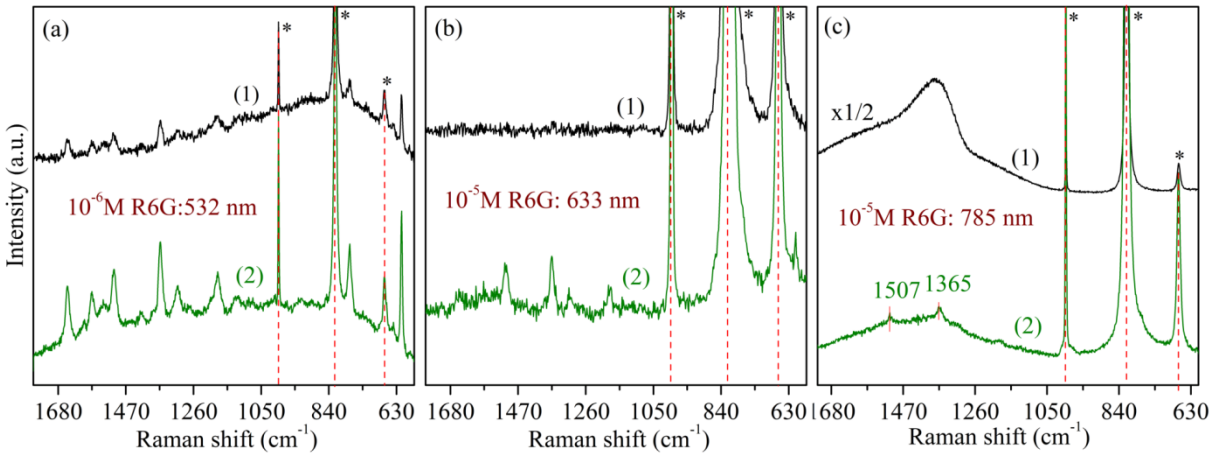

Fig. S7 SERS spectra of R6G on α-MoO_3 MPs without (1) and with (2) oxygen vacancies excited with (a) 532, (b) 633 and (c) 785 nm lasers. The oxygen vacancies were introduced by heat treatment at 473 K in vacuum for 1 h.

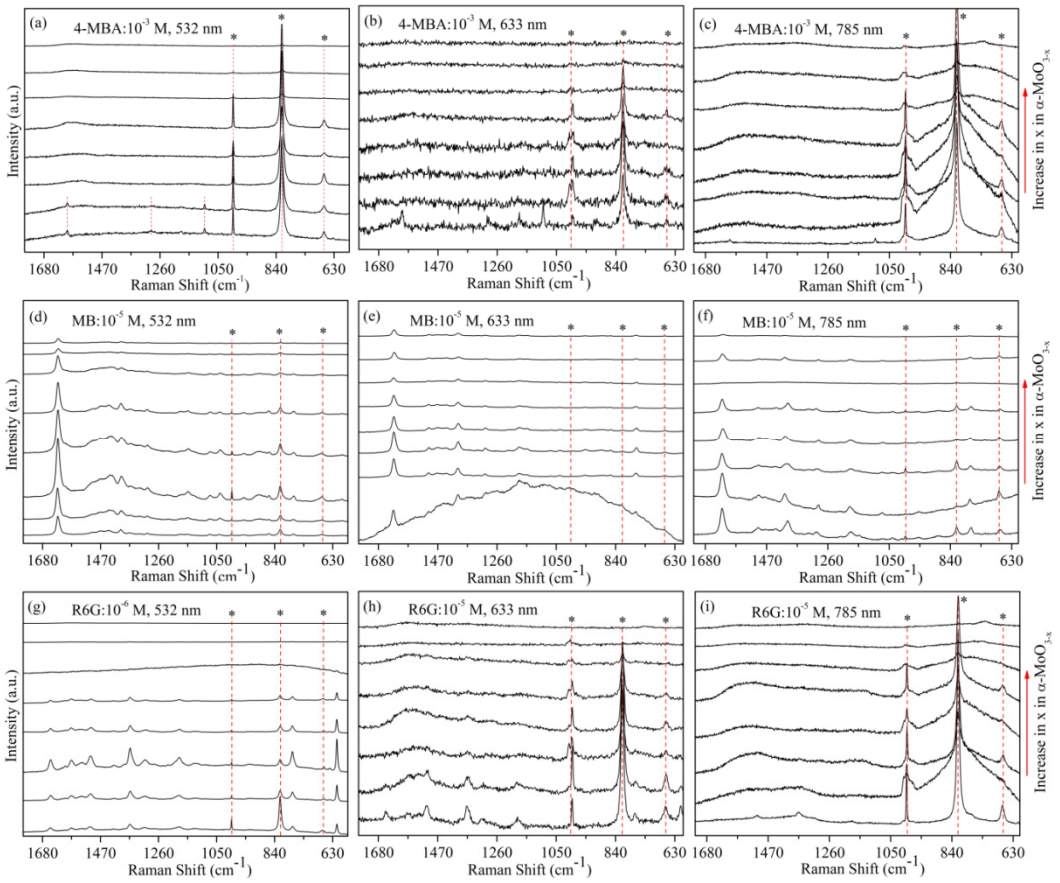

Fig. S8 SERS spectra of 4-MBA, MB and R6G on α-MoO_{3-x} nanobelts with different oxygen vacancy concentrations excited with 532, 633 and 785nm laser

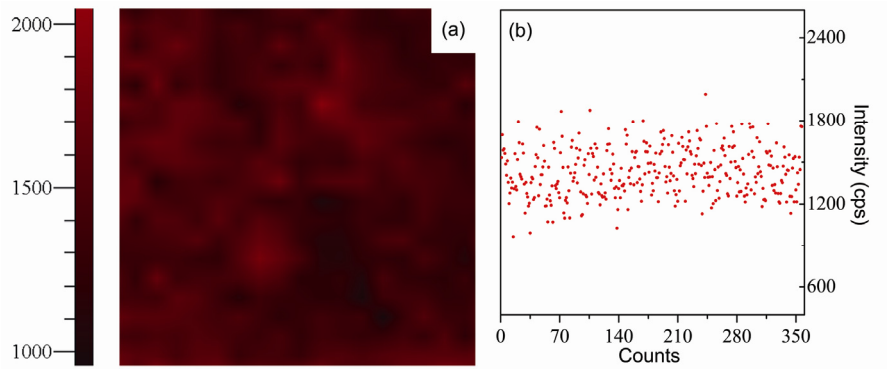

Fig. S9 Point-to-point SERS mapping image (a) and the corresponding SERS intensity (b) of 10^{-6} M R6G over on α-MoO_{3-x} nanobelts substrates at 614 cm^{-1} excited with 532 nm laser. The effective laser power is 0.3 mW with each data point at a single record of 1s. The standard deviation of the measurements in (b) is about 12.2 %.

5. SERS activity of α-V_2O_5

α-V_2O_5 is a orthorhombic $3d^0$ V(V) insulator with a band gap of ~2.80 eV. The work function of stoichiometric α-V_2O_5 is ~7.86 eV.[7, 15, 21] The schematic diagram for the energy levels of stoichiometric α-V_2O_5 and R6G is shown in Scheme S7a.[7, 15] Carriers in stoichiometric α-V_2O_5 cannot be excited by incident light longer than 443 nm (2.80 eV). Oxygen vacancy defects are used to introduce new energy levels in α-V_2O_5 and all the α-V_2O_5 samples are surface-clean without surfactants. The energy levels of oxygen vacancy defects will appear

within the energy gap, and the carriers in V_2O_5 can be excited by visible light and matching with the HOMO (-5.70eV) and LUMO (-3.40eV) of R6G excited with three lasers.[14]

The PICT process in the system of α-V_2O_{5-x} and R6G excited with three lasers before and after introducing oxygen vacancy are shown in Table S2. After introduction of oxygen vacancy, a strong CT_1 will join the PICT process excited with 532 nm laser, which will enhance the Raman signals obviously, while a relatively weak CT_2 will appear in the PICT process excited with 633 and 785 nm lasers.

The stoichiometric micron-sized α-V_2O_5 particles (α-V_2O_5 MPs) was prepared by calcinating commercial V_2O_5 (A. R. grade) at 873 K in air for 5h and then selected through centrifugation in ethanol and dried at 353 K for 12 h. α-V_2O_5 nanoparticles (NPs) were synthesized by hydrothermal method, followed by the calcination at 723 K in air for 1 h (NPs sample a). Some of the nanoparticles were annealed in vacuum at 373 and 473 K for 1 h as NPs sample b and c, respectively.

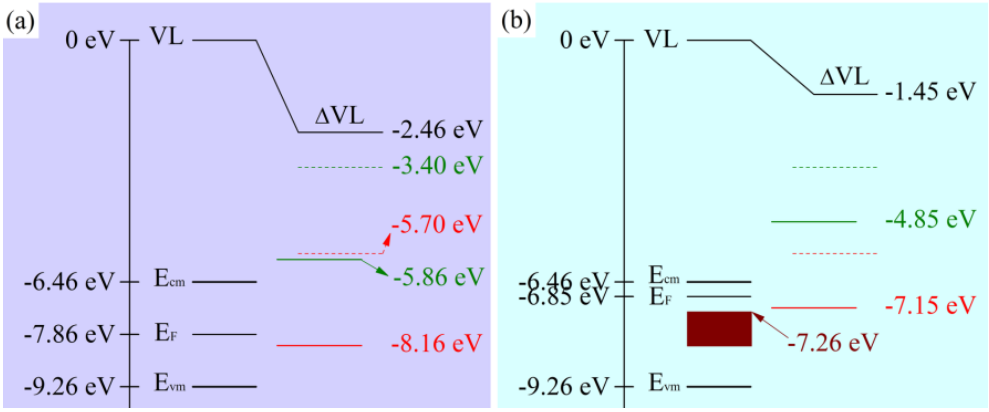

Scheme S7. Energy diagrams for R6G on α-V_2O_5 before (a) and after (b) introduction of defect levels. The olive line refers the LUMO and red line the HOMO, the wine area represents the energy levels of oxygen vacancy. The dashed lines represent the LUMO and HOMO of MB and R6G with vacuum levels alignment.

Table S2. Energy level matching and CT process of R6G on α-V_2O_5 MPs and α-V_2O_{5-x} NPs with different laser wavelengths.

Laser wavelength (nm)	α-V_2O_5 MPs		α-V_2O_{5-x} NPs	
	Energy matching	CT process	Energy matching	CT process
532 (2.33 eV)	$h\nu>E_{LUMO}-E_{HOMO}$ $h\nu>E_{cm}-E_{HOMO}$	CT_3	$h\nu>E_{cm}-E_{vm}$ $h\nu>E_{LUMO}-E_{HOMO}$ $h\nu>E_{cm}-E_{HOMO}$	CT_1 CT_3
633 (1.96eV)	None	None	$h\nu>E_{cm}-E_{vm}$	CT_2
785 (1.58eV)	None	None	$h\nu>E_{cm}-E_{vm}$	CT_2

XRD analysis (Fig. S10) shows that the α-V_2O_5 MPs and α-V_2O_5 NPs are all pure α-V_2O_5. Fig. S11 shows FESEM image of α-V_2O_5 MPs and NPs. α-V_2O_5 MPs has an average size of several tens of microns, while α-V_2O_5 NPs have an average size of about 100 nm. XPS analysis indicates that the oxygen vacancy defects in α-V_2O_5 MPs is negligible (Fig. S12a), while the concentration of oxygen vacancy increases with increasing annealing temperatures (Fig. S12b-d). Table S3 shows the x value of three α-V_2O_{5-x} NPs samples calculated from XPS results. The difference in the adsorbance on these three NPs samples is also very small and the influence on SERS can be ignored.

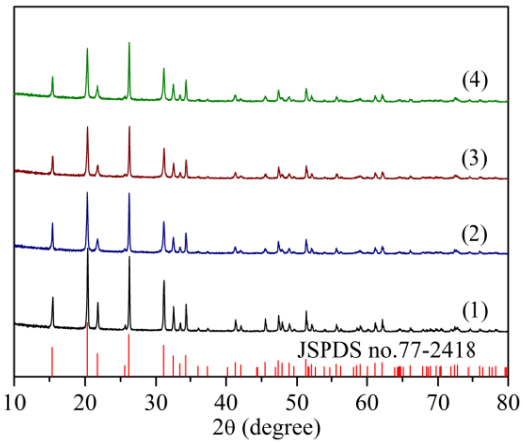

Fig. S10 XRD pattern of α-V_2O_5: curve (1) MPs, (2) NPs sample a, (3) NPs b and NPs c together with that from standard α-V_2O_5 JSPDS no. 77-2418.

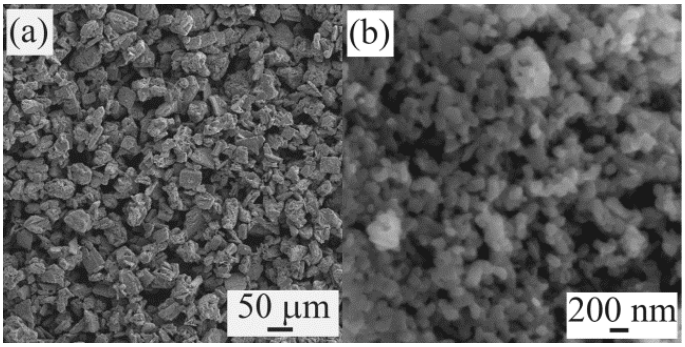

Fig. S11 FESEM images of α-V_2O_5 (a) micro-sized particles and (b) nanoparticles.

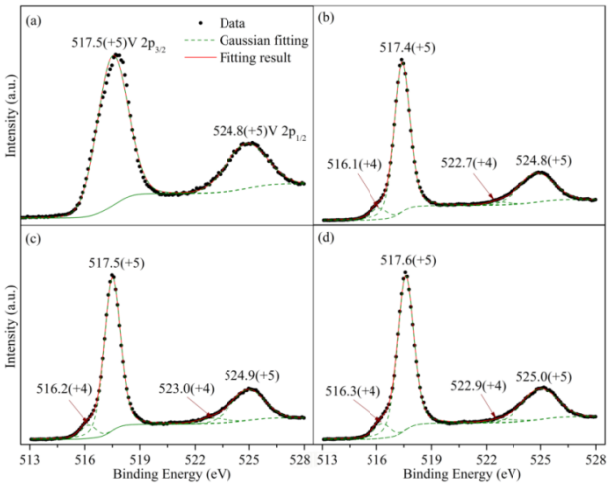

Fig. S12 XPS spectra of V 2p and the corresponding Gaussian fitting of (a) α-V_2O_5 MP and (b-d) α-V_2O_{5-x} NPs. The peak components for V^{5+} and V^{4+} are indicated.

Table S3. Preparation condition and x value of α-V_2O_{5-x} NPs calculated from XPS results

V_2O_{5-x} NPs	Preparation condition	x values
a	calcination at 723K in air for 1 h (A)	0.06472
b	A + annealing in vacuum at 373K for 1 h	0.07045
c	A + annealing in vacuum at 473 K for 1 h	0.07933

Fig. S13 shows the Raman spectra of α-V_2O_5 MPs and α-V_2O_{5-x} NPs. Excited with 532 nm laser, no molecular Raman signals can be observed for R6G on α-V_2O_5 MPs with the concentration less than 10^{-5} M (appears with 10^{-5} M), while they appear for R6G on α-V_2O_{5-x} NPs with the concentration of 10^{-6} M (Fig. S13a). Excited with 633 and 785 nm lasers, no molecular Raman signals can be seen for R6G on α-V_2O_5 MPs with the concentration of 10^{-5} and 10^{-4} M, respectively, and yet obvious SERS signals occur on α-V_2O_{5-x} NPs (Fig. S13b and c).

The SERS intensity of R6G increases with increasing x value in α-V_2O_{5-x} NPs, which is in agreement with the prediction shown in Table S2 that the PICT process contains both CT_1 and CT_3 excited with 532 nm laser, and contains CT_2 excited with 633 and 785 nm lasers, as shown in Fig. S14. These results clearly demonstrate that oxygen vacancy defects can enhance the SERS effect of α-V_2O_{5-x} NPs with 532 nm laser and turn α-V_2O_{5-x} NPs from non-SERS substrate to SERS active substrate with 633 and 785 lasers for R6G.

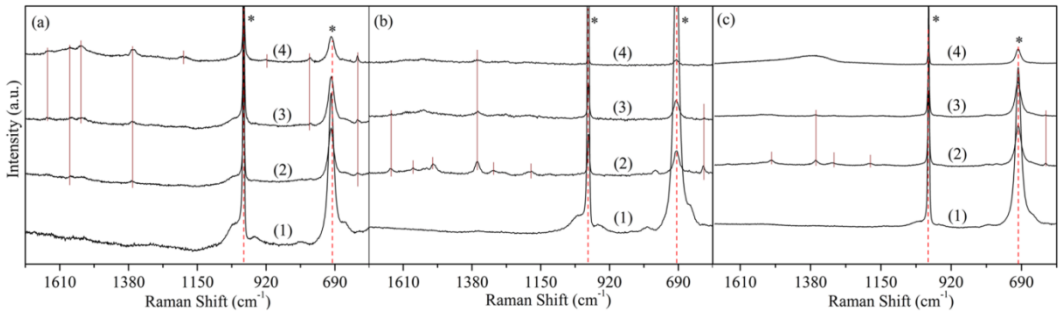

Fig. S13 SERS spectra of R6G on V_2O_5 MPs and NPs. (a) 10^{-6} M with 532 nm laser, (b) 10^{-5} M with 633 nm laser, and (c) 10^{-4} M with 785 nm laser. The * refers to the Raman peaks from α-V_2O_5.

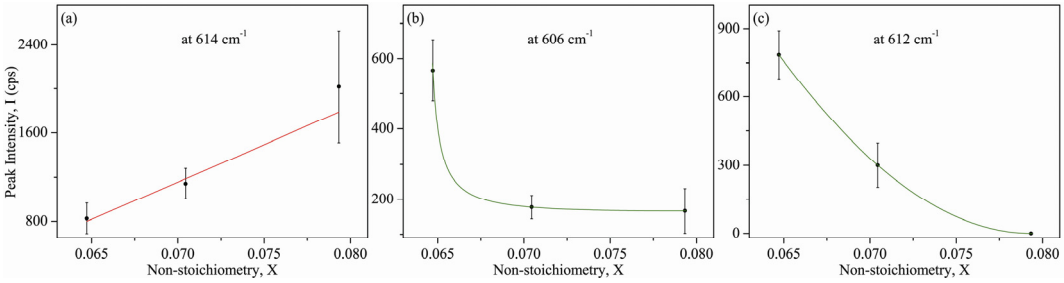

Fig. S14 Raman intensity of R6G characteristic as a function of non-stoichiometry in α-V_2O_{5-x} NPs excited with laser wavelength of (a) 532, (b) 633 and (c) 785 nm. The solid lines are fitting results.

6. Calculation of HOMO and LUMO energy levels of MB molecule

The absorption spectrum of 10^{-5} M MB aqueous solution is shown in Fig. S15. The background absorbance was eliminated by introducing deionized water as a reference. The band gap of the MB molecule is evaluated from the absorbance spectrum using the relations: $\alpha h\nu = A_0(h\nu - E_g)^{1/2}$, here α is the absorption constant, $h\nu$ and E_g are photon energy and direct energy band gap, respectively, and A_0 is a constant, and the result is shown in the inset of Fig. S15, from the intercept of the straight line to the $h\nu$ axis gives, we can get the bandgap energy of the MB molecules is about 1.81 eV. The LUMO of MB is -0.231V vs SCE,[22] i.e. LUMO=-(-0.23+4.74)=-4.51eV, and thus HOMO=LUMO–E_g=-4.51–1.81=-6.32eV.

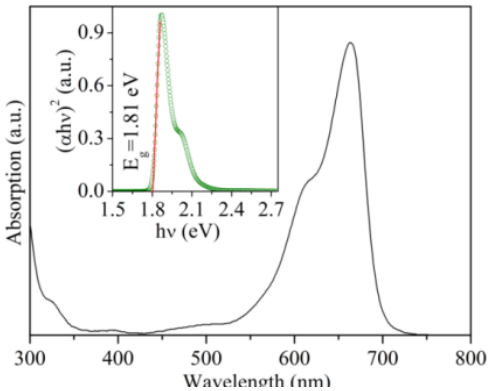

Fig. S15 UV–Vis absorption spectrum of MB aqueous solution. The inset is a plot of $(\alpha h\nu)^2$ vs. hν.

7. Calculation of the enhancement factor

The Calculation of the enhancement factor (*EF*) is calculated by comparing the ratio of the Raman peak intensity absorbed molecules on α-MoO_{3-x} nanobelts (I_{SERS}) to pure molecular Raman signal on glass substrate (I_{RS}) using the equation:

$$EF = \frac{I_{SERS} / N_{SERS}}{I_{RS} / N_{RS}} \tag{S7-1}$$

where N_{SERS} and N_{RS} represent the number of molecules on α-MoO_{3-x} nanobelts and glass within the laser spot, respectively. Since the areas of the laser spot are the same, *EF* can be approximately calculated by

$$EF = \frac{I_{SERS}}{I_{RS}} \frac{S_{SERS} V_{RS} C_{RS}}{S_{RS} V_{SERS} C_{SERS}} \tag{S7-2}$$

A certain volume V_{RS} and concentration C_{RS} of the adsorbate solution was dispersed onto an area of S_{RS} on glass, and dried to form solid thin film as the reference. A certain volume V_{SERS} and concentration C_{SERS} of the adsorbate solution was absorbed on α-MoO_{3-x} nanobelts, which were then rinsed and dispersed onto an area of S_{SERS} on glass. Since the excess molecules on α-MoO_{3-x} nanobelts have been rinsed off while those on the glass substrates have not, the *EF* calculated here is somewhat smaller than the actual one. The detection limit was determined by the lowest detectable Raman signal of the molecules. The Raman measurement results are omitted here, and the enhancement factor and detection limit are shown in Table S4. Although α-MoO_{3-x} is a SERS-active substrate for 4-MBA in 633nm, no signals can be found for 4-MBA molecular Raman, and thus no EF can be obtained.

Table S4. Enhancement factor (*EF*) and detection limit (Γ) of α-MoO_3 nanobelts and MPs, and *x* value in α-MoO_{3-x} nanobelts

Molecule (characteristic peak, cm^{-1})	Laser (nm)	α-MoO_3 MPs		α-MoO_{3-x} nanobelts		
		EF	Γ(M)	*EF*	Γ(M)	x value
4-MBA (1595)	532	/	/	295	10^{-3}	~0
	633	/	/	N/0	10^{-3}	~0
	785	/	/	330	10^{-3}	~0
MB (1626)	532	5.7×10^4	10^{-6}	1.0×10^6	10^{-7}	0.01851
	633	6.7×10^4	10^{-5}	9.5×10^5	10^{-6}	0.01851
	785	/	/	2.9×10^5	10^{-6}	~0
R6G (612)	532	9.3×10^5	10^{-6}	1.8×10^7	10^{-8}	0.01851
	633	/	/	3.0×10^5	10^{-6}	~0
	785	/	/	2.4×10^3	10^{-5}	~0

8. Potential metal oxide SERS-active substrates

Scheme S8 shows the energy diagram and sub-PICT processes of R6G on some potential metal oxide SERS-active substrate excited with three lasers. All the predictions are based on the assumption that γ=0 and R6G molecules are adsorbed tightly to the substrate. We only consider only the possible thermodynamics process. In reality the dynamics process might also take certain role. The SERS performance and mechanism can be predicted based on our model, and the results are listed in Table S5. One can see that the stoichiometric Cr_2O_3, CrO_3, CoO, NiO and Ta_2O_5 are SERS-active for R6G only with 532 nm laser, and Co_3O_4 is SERS-active for R6G with all three lasers. The SERS-activity of R6G with 532 nm laser over CrO_3 and Ta_2O_5 will be enhanced, and Cr_2O_3 and Ta_2O_5 will be transferred from non-SERS to SERS active for R6G with 633 and 785 nm lasers by introducing oxygen vacancy defects.

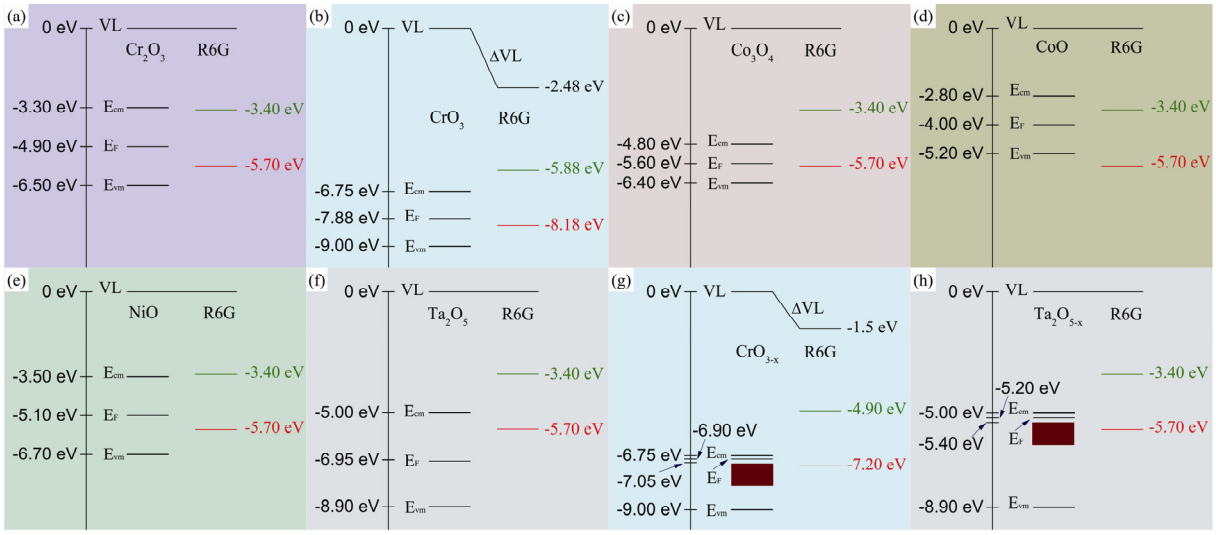

Scheme S8. Energy diagram of R6G on the substrate of (a) Cr_2O_3, (b) CrO_3, (c) Co_3O_4, (d) CoO, (e) NiO and (f) Ta_2O_5 (g) CrO_{3-x} (h) Ta_2O_{5-x}. The energy levels of the substrates are from reference.[7] The olive line refers the LUMO and red line the HOMO, the wine area represents the energy levels of oxygen vacancy.

Table S5. Energy level matching and sub-PICT process of R6G adsorbed on the substrate with different laser wavelengths.

Substrate	532 nm			633 nm			785 nm		
	Energy matching	sub-PICT process	SERS intensity I(x)	Energy matching	sub-PICT process	SERS intensity I(x)	Energy matching	sub-PICT process	SERS intensity I(x)
Cr_2O_3	$h\nu>E_{LUMO}-E_{HOMO}$ $h\nu>E_{cm}-E_{HOMO}$	CT_3	/	None	None	None	None	None	None
CrO_3	$h\nu>E_{cm}-E_{vm}$ $h\nu>E_{LUMO}-E_{HOMO}$ $h\nu>E_{cm}-E_{HOMO}$	CT_2 CT_3	/	None	None	None	None	None	None
Co_3O_4	$h\nu>E_{cm}-E_{vm}$ $h\nu>E_{LUMO}-E_{HOMO}$ $h\nu>E_{cm}-E_{HOMO}$	CT_2 CT_3	/	$h\nu>E_{cm}-E_{vm}$	CT_2	/	$h\nu>E_{cm}-E_{vm}$	CT_2	/
CoO	$h\nu>E_{cm}-E_{vm}$	CT_1	/	None	None	None	None	None	None
NiO	$h\nu>E_{LUMO}-E_{HOMO}$ $h\nu>E_{cm}-E_{HOMO}$	CT_3	/	None	None	None	None	None	None
Ta_2O_5	$h\nu>E_{LUMO}-E_{HOMO}$ $h\nu>E_{cm}-E_{HOMO}$	CT_3	/	None	None	None	None	None	None
CrO_{3-x}	$h\nu>E_{cm}-E_{vm}$ $h\nu>E_{LUMO}-E_{HOMO}$ $h\nu>E_{cm}-E_{HOMO}$	CT_1 CT_3	$I=a\varphi(x)x+b$	$h\nu>E_{cm}-E_{vm}$	CT_2	$I=\frac{x^2+a_1x+a_2}{b_1x+b_2}$	$h\nu>E_{cm}-E_{vm}$	CT_2	$I=\frac{x^2+a_1x+a_2}{b_1x+b_2}$
Ta_2O_{5-x}	$h\nu>E_{cm}-E_{vm}$ $h\nu>E_{LUMO}-E_{HOMO}$ $h\nu>E_{cm}-E_{HOMO}$	CT_1 CT_3	$I=a\varphi(x)x+b$	$h\nu>E_{cm}-E_{vm}$	CT_1	$I=a\varphi(x)x+b$	$h\nu>E_{cm}-E_{vm}$	CT_2	$I=\frac{x^2+a_1x+a_2}{b_1x+b_2}$

9. Evidence of SERS-activity from chemical enhancement mechanism

The obvious shift of the characteristic Raman peaks and the vibration dependence of the enhancement factors are the convincing evidences for the PICT process in the chemical enhancement mechanism,[14, 23] see Fig. S16. The peak shifts derived from Fig. S16 are listed in Table S6. Taking the result of R6G in 532 nm as an example, it was found that *EF* is 1.35×10^7, 1.75×10^7 and 4.46×10^6 at 771, 611 and 1643 cm^{-1}, respectively. The nearly planar xanthene ring of R6G lies flat on the surface of the substrate, which can be considered as a plane of symmetry. The in-plane vibrations are totally symmetric (a') and the out-of-plane vibrations are not totally symmetric (a'') according to the symmetry point group C_s. Since the charge-transfer transition dipole is perpendicular to the molecular plane, the a'' vibrations at 611 cm^{-1} and 773 cm^{-1} will be more selectively enhanced.[14]

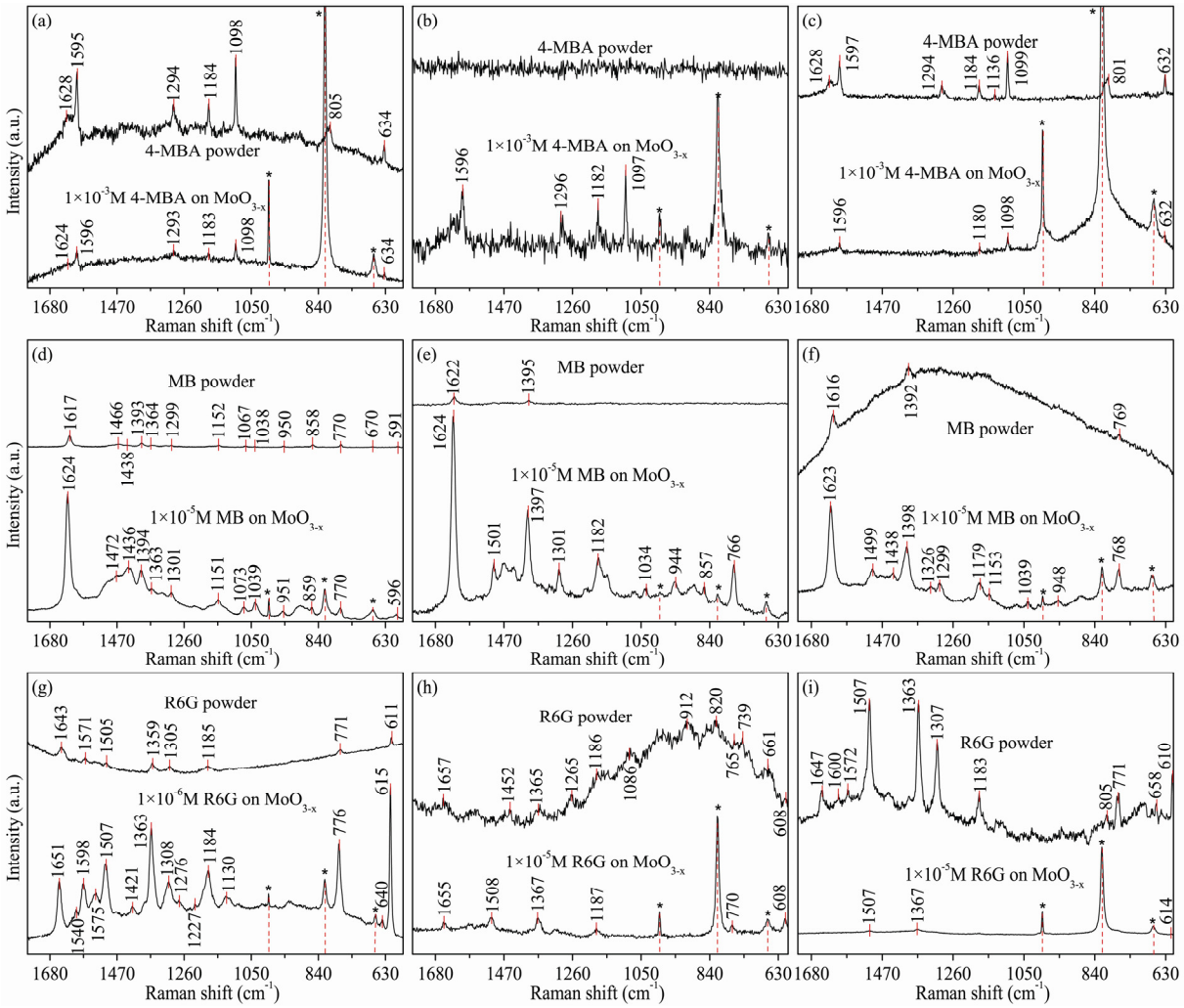

Fig S16 The comparison between NRS spectra and the SERS results of the adsorbate absorbed on α-MoO_{3-x} nanobelts after the optimization of oxygen vacancy defects with different lasers. 4-MBA with (a) 532, (4) 633 and (c) 785 nm lasers. MB with (d) 532, (e) 633 and (f) 785 nm laser. R6G with (g) 532, (h) 633 and (i) 785 nm laser. The curves have been moved vertically. The * refers to the Raman peaks from α-MoO_3. The molecular characteristic peak and molar concentration are indicated.

Table S6. The obvious shift of the characteristic Raman peaks from Fig. S16.

molecules	Laser (nm)	Peak position in NRS (cm^{-1})	Peak position in SERS spectrum (cm^{-1})
4-MBA	532	1628	1624
	633	No signals	/
	785	1184	1180
MB	532	1617	1626
		1067	1073
		591	596
	633	1622	1626
	785	1616	1623
		1392	1398
R6G	532	1643	1651
		1571	1575
		1359	1363
		771	776
		611	615
	633	765	770
	785	1363	1367
		610	614

References

1 A. C. Albrecht, *J. Chem. Phys.*, 1961, **34**, 1476-1484.

2 J. R. Lombardi and R. L. Birke, *J. Phys. Chem. C*, 2008, **112**, 5605-5617.

3 J. R. Lombardi, R. L. Birke, T. Lu and J. Xu, *J. Chem. Phys.*, 1986, **84**, 4174-4180.

4 B. N. J. Persson, K. Zhao and Z. Zhang, *Phys. Rev. Lett.*, 2006, **96**, 207401.

5 X. Wang, W. Shi, G. She and L. Mu, *J. Am. Chem. Soc.*, 2011, **133**, 16518-16523.

6 J. R. Lombardi and R. L. Birke, *J. Phys. Chem. C*, 2014, **118**, 11120-11130.

7 M. T. Greiner, M. G. Helander, W. M. Tang, Z. B. Wang, J. Qiu and Z. H. Lu, *Nat. Mater.*, 2012, **11**, 76-81.

8 L. Ley, Y. Smets, C. I. Pakes and J. Ristein, *Adv. Funct. Mater.*, 2013, **23**, 794-805.

9 L. Chai, R. T. White, M. T. Greiner and Z. H. Lu, *Phys. Rev. B*, 2014, **89**, 035202.

10 S. Cong, Y. Yuan, Z. Chen, J. Hou, M. Yang, Y. Su, Y. Zhang, L. Li, Q. Li, F. Geng and Z. Zhao, *Nat. Commun.*, 2015, **6**, 7800.

11 J. R. Lombardi and R. L. Birke, *J. Chem. Phys.*, 2007, **126**, 244709.

12 L. B. Yang, P. Li, H. L. Liu, X. H. Tang and J. H. Liu, *Chem. Soc. Rev.*, 2015, **44**, 2837-2848.

13 I. V. Krive, A. Palevski, R. I. Shekhter and M. Jonson, *Low Temp. Phys.*, 2010, **36**, 119-141.

14 X. Wang, W. Shi, G. She and L. Mu, *J. Am. Chem. Soc.*, 2011, **133**, 16518-16523.

15 M. T. Greiner, L. Chai, M. G. Helander, W. M. Tang and Z. H. Lu, *Adv. Funct. Mater.*, 2012, **22**, 4557-4568.

16 D. Li, B. H. O'Connor and H. Sitepu, *J. Appl. Crystallogr.*, 2005, **38**, 158-167.

17 D. O. Scanlon, G. W. Watson, D. J. Payne, G. R. Atkinson, R. G. Egdell and D. S. L. Law, *J. Phys. Chem. C*, 2010, **114**, 4636-4645.

18 X. L. Li, J. F. Liu and Y. D. Li, *Appl. Phys. Lett.*, 2002, **81**, 4832-4834.

19 X. W. Lou and H. C. Zeng, *Chem. Mater.*, 2002, **14**, 4781-4789.

20 T. He, Y. Ma, Y. Cao, P. Jiang, X. Zhang, W. Yang and J. Yao, *Langmuir*, 2001, **17**, 8024-8027.

21 S. Laubach, P. C. Schmidt, Thi, F. J. Fernandez-Madrigal, Q. H. Wu, W. Jaegermann, M. Klemm and S. Horn, *Phys. Chem. Chem. Phys.*, 2007, **9**, 2564-2576.

22 J. Huang, Z. Huang, Y. Yang, H. Zhu and T. Lian, *J. Am. Chem. Soc.*, 2010, **132**, 4858-4864.

23 X. Ling, L. Xie, Y. Fang, H. Xu, H. Zhang, J. Kong, M. S. Dresselhaus, J. Zhang and Z. Liu, *Nano Lett.*, 2010, **10**, 553-561.